THE FLORIDA STATE UNIVERSITY

COLLEGE OF ARTS AND SCIENCES

BETA DECAY STUDIES OF NEUTRON-RICH ^{30,31}AL AND IN-BEAM STUDIES OF NEUTRON-RICH ^{30}AL.

By

TRISHA HINNERS

A Dissertation submitted to the
Department of Physics
in partial fulfillment of the
requirements for the degree of
Ph.D.

Degree Awarded:
Spring Semester, 2008

The members of the Committee approve the Dissertation of Trisha Hinners defended on

Samuel L. Tabor
Professor Directing Dissertation

Ettore Aldrovandi
Outside Committee Member

Susan Blessing
Committee Member

Mark Riley
Committee Member

Jorge Piekarewicz
Committee Member

Approved:

Mark Riley, Chair
Department of Physics

Joseph Travis, Dean, College of Arts and Sciences

The Office of Graduate Studies has verified and approved the above named committee members.

Dedication

To Dad for his constant encouragemnt, Mom for lending an ear, Katie for being a voice of realism, and Hill for his unending support.

ACKNOWLEDGEMENTS

This work was supported in part by the U.S. National Science Foundation under grants PHY-01-39950, PHY-01-10253, and PHY-04-56463. We wish to thank Y. Utsuno for valuable discussions, the NSCL staff for smooth running of the accelerator, and Powell Barber for fabrication of the ^{18}O target.

TABLE OF CONTENTS

LIST OF TABLES

LIST OF FIGURES

ABSTRACT

Low-spin states were studied in ^{30}Al following the β decay of ^{30}Mg produced in the fragmentation of 140 MeV/AMU ^{48}Ca. Analysis of the β-γ and β-γ-γ coincidences revealed a new 1^+ state at 2413 keV, confirmation of the level scheme, and a more accurate half life measurement of 315(6) ms for the ^{30}Mg ground state. Higher-spin states were investigated in the reaction of ^{14}C on ^{18}O at 22 MeV. Protons and deuterons were detected in a segmented E-ΔE Si telescope in coincidence with one or two γ rays in the FSU Ge detector array. A comparison of the resulting level and decay scheme with predictions of the *sd* shell model shows good agreement with all but 6 of the states in both excitation energy and γ decay branching ratios. The RMS deviations in energy of these states using the older USD and newer USDA and USDB interactions were 265, 176, and 173 keV respectively. The remaining 6 states are well described as 4^- to 7^- states, similar in relative energy to those in ^{28}Al but shifted down by about 1200 keV. These states also agree well with the predictions of shell model calculations using the WBP interaction. A comparison of the lowest 4^- states in even A Na, Al, and P isotopes shows a systematic decrease in energy with increasing N and with decreasing Z. The energies of the 4^- states are almost identical in nuclei with the same N - Z values.

In addition to the study of ^{30}Al, ^{31}Al was also produced following the β decay of ^{31}Mg in the fragmentation of 140 MeV/AMU ^{48}Ca. The β-γ and β-γ-γ coincidences were able to show all previously known work. However, no new transitions were observed.

CHAPTER 1

Introduction

The existence of intruder states at high excitation energies based on configurations involving orbitals outside the shell being filled comes as no surprise. However, their presence at low excitations and even in the ground states (g.s.) of neutron-rich nuclei has been surprising at times and continues to challenge theoretical understanding. One of the early surprises was the unexpected $\frac{1}{2}^+$ g.s. of ^{11}Be [1] when the seventh neutron is expected to occupy the $p_{1/2}$ orbital. Fig. 1 in Ref. [1] illustrates another important characteristic, namely the fact that the position of the neutron intruder state depends not only on the number of neutrons, but also on the number of protons. The position of the $\frac{1}{2}^+$ intruder state falls with decreasing Z even for constant N.

For the normal states, the demonstration that one effective interaction with smooth A dependence (USD) [2, 3] can describe most of the structure observed in the *sd* shell was one of the early successes of the large-basis shell model. Since the interaction was fitted to the known states throughout the shell, it may include some of the effects of two-particle two-hole intruder configurations. The failures of a model can be as instructive as its successes. The failure to reproduce the g.s. binding energy of ^{31}Na, while giving excellent agreement for the lighter isotopes [4], was an early indication for intruder configurations in the g.s. of some *sd* shell nuclei that are not well reproduced by calculations employing the USD effective interaction. This region of nuclei with Z near the bottom of the *sd* shell and N near the top, where the energies of intruder-dominated configurations fall below those of the normal configurations, has been called the "island of inversion." Recent studies have traced out the decreasing energies of intruder configurations with increasing N in the Na isotopes [5, 6, 7].

Recently new *sd* effective interactions (USDA and USDB) have been derived by fitting the greatly expanded structure now known in *sd* shell nuclei [8]. Even though considerably

more levels in neutron-rich nuclei were included in adjusting the new interactions, the underprediction of the binding energies of nuclei in the island of inversion remains. Inversion effects are reasonably accounted for in calculations including the fp shell, *e.g.* by using the SDPF-M interaction which involves a Z and N dependent shell gap [9].

The present work on ^{30}Al was initiated to see whether the newer *sd* effective interactions provide a better description of a neutron-rich nucleus not involved in the adjustment and to provide further information on the behavior of intruder structures as a function of N and Z approaching the island of inversion. Complementary approaches were used: Low-spin states were explored following the β decay of the 0^+ g.s. of ^{30}Mg produced in the fragmentation of ^{48}Ca, and high-spin states were investigated by detecting particle-γ coincidences in a heavy-ion reaction involving a long-lived radioactive beam.

Excited states were previously observed in ^{30}Al in the ^{30}Si(t,^{3}He) reaction [10, 11, 12], following the β decay of ^{30}Mg [13, 14] and in a particle-γ coincidence experiment with the ^{14}C(^{18}O,pn) reaction [15]. An early suggestion that the first excited state is isomeric was ruled out by subsequent work. Also a tentative state at 1000(30) keV [10] or 991 keV [15] was not seen in other experiments and will be discussed in this paper.

^{31}Al was investigated via β decay of the $\frac{1}{2}^+$ g.s. of ^{31}Mg produced only in the previously mentioned β decay experiment, and was of interest due to its location bounding the island of inversion. Excited states were previously observed in ^{31}Al by [16, 17]. In addition, the ground state spin and magnetic moment were determined by [18].

CHAPTER 2

Theory

2.1 Beta Decay

The most basic β decay process in a nucleus is the conversion of a proton into a neutron or a neutron into a proton. In a nucleus, β decay changes N and Z by one such that, Z $\rightarrow$ Z$\pm$ 1, N $\rightarrow$ N$\mp$1, and A = Z + N remains constant. It can be said then that β decay offers an unstable nucleus a really convenient way to become a stable isobar. There are three different versions of beta decay. Negative β decay where the β is an ordinary electron and represented by β^-, n $\rightarrow$ p + β^- + $\overline{\nu}_e$ (this is also the type of β decay to be discussed in this dissertation), positive β decay, where p $\rightarrow$ n + β^+ + ν_e, and orbital electron capture p + e^- $\rightarrow$ n + ν_e. The weak force is the fundamental force responsible for this change of a neutron into a proton with the emission of an electron and an antineutrino, or in the case of positive β decay, the transmutation of a proton into a neutron and the emission of a positron and a neutrino, both as described above.

2.1.1 Fermi Theory of Beta Decay

Enrico Fermi came up with a simple way to describe β decay in 1934 based on Pauli's neutrino hypothesis. The main aspects of the decay can be derived from the expression for the transition probability caused by an interaction that is weak compared with the interaction that forms the quasi-stationary states. This is consistent with the observation that β-decay half-lives are typically longer on the order of seconds compared to typical nuclear decay times. This observation led to a calculation that treated the decay-causing interaction as a weak perturbation. This became known as Fermi's Golden Rule, and gives a general result for the transition rate, where $\rho(E_f)$ is the density of states,

$$\lambda = \frac{2\pi}{\hbar}|M_{fi}|^2\rho(E_f).$$

The matrix element M_{fi} is the integral of the interaction M between the initial and final quasi-stationary states of the system,

$$M_{fi} = \int \Psi_f^* M \Psi d^3r.$$

The factor of $\rho(E_f)$ is the density of available states, suggesting that a transition is more likely to occur if there is a large number of final states.

However, Fermi came to his results considering special relativity and showed that V could be replaced with one of 5 operators, a vector, axial vector, scalar, pseudoscalar, or a tensor. After experimental findings gathered over 20 years, the symmetries and the spatial properties of the decay products were found to deduce to the proper vector-axial form (V-A),

$$|M_{fi}|^2 = \Sigma|\int \Psi_f^*(\Sigma\tau_\pm^k)\Psi_i d^3r|^2,$$

where the operators $\tau_+ = \tau_x + i\tau_y$ and $\tau_- = \tau_x$ - $i\tau_y$ are the Pauli (raising and lowering) operators for isospin. The operator τ_+ transforms a neutron into a proton and is used in β^- decay, and τ_- has the opposite effect and is used in β^+ decay. Since the force carrying particle for the weak interaction of interest, W^-, acts in combination with τ_+ we can say then that the effective current operator that couples to the W^- is ,

$$J^\mu = \bar{\Psi}_L(x)\gamma^\mu\Psi_L,$$

The hallmark of this weak interaction is parity violation. Therefore only left-handed particles can participate in the weak interaction. In the non-relativistic limit the current operator reduces to,

$$J^o = \rho = \tau_+(Fermi\ Operator)$$

$$\vec{J} = \vec{\sigma}\tau_+(Gamow - Teller\ Operator)$$

which essentially changes the neutron into a proton. This suggests two types of β-decay transitions. First, the Fermi transitions change the isospin by one but leaves all other quantum numbers unchanged. For example a $J^\pi = 0^+$ nucleus for a Fermi transition can only decay into a $J^\pi = 0^+$ state in the daughter nucleus. In the case of the Gamow-Teller transition,the change in isospin is exactly as in the Fermi transition, but the angular

momentum of the daughter state may differ from the parent state by one unit, while the parity remains unchanged. An example of this is a $J^\pi = 0^+$ nucleus that Gamow-Teller transitions into daughter states of $J^\pi = 1^+$.

2.1.2 Log *ft* Values

The decay constant λ can be written as,

$$\lambda = \frac{m^5 g^2 c^4 |M_{if}|^2}{2\pi^3 \hbar^7} f(Z, E_T),$$

where,

$$f(Z, E_T) = \frac{1}{m^5 c^{10}} \int_0^{E_T} F(Z, E) E (E^2 - m^2 c^4)^{1/2} (E_T - E)^2 dE,$$

which is known as the Fermi integral.

This equation gives information on how the matrix element M_{if} effects the evaluation of the decay constant λ. Using the relationship,

$$t_{1/2} = \frac{ln2}{\lambda},$$

the expression for λ can be rewritten as,

$$ft_{1/2} = \frac{1.386\pi^3 \hbar^7}{g^2 m^5 c^4 |M_{if}|^2}.$$

From this information, $ft_{1/2}$ really only depends on the matrix element. Therefore, the larger M_{if} is, the more probable a transition. Transitions where M_{if} is near 1 produce the lowest ft values and are called *superallowed*. Similarly, transitions where the ft value is much larger than the allowed values are known as forbidden, therefore much less likely to occur. What this means is by calculating log *ft* values the allowedness of various transitions can be determined, helping understand the decay paths and their J^π in a more complete way.

2.2 Single Particle Shell Model

Looking for a better way to describe nuclear structure, nuclear physicists looked to the successful atomic shell model for guidance. In the atomic shell model, shells are filled with

electrons in order of increasing energy according to the Pauli principle. When this occurs, an inert core of filled shells and some number of valence electrons are obtained. The model assumes that the valence electrons are responsible for determining atomic properties. The agreement with measurements of atomic properties with theory predictions is extremely good. In particular, regular and smooth variations of the atomic properties occur within a subshell, while drastic changes occur when one subshell is filled and electrons begin to enter the next subshell.

This model was carried over to nuclear physics and there were several immediate issues that needed to be understood to implement it successfully. For the atomic shell model, the potential comes from the Coulomb field of the nucleus and the subshells or orbits are determined by external sources. The Schrodinger equation can be solved for this potential, and energies of the subshells where the electrons reside can be determined. In a nucleus, however, no external source exists, and the nucleons move in a potential created by the nucleons themselves. Another issue was the existence of spatial orbits in atomic theory. This allows the electrons to move around in those orbits freely without bumping into other electrons. Nucleons are much larger in diameter compared to the size of the nucleus, than electrons to the atom, so it's difficult to describe orbits where the nucleons do not make too many collisions with other nucleons.

So why did early nuclear physicists think that the atomic shell model would be a good basis for understanding nuclear structure? The first bit of evidence can be found from observing the measured proton and neutron separation energies. Figure 2.1 adapted from Ref. [19] shows the measured proton and neutron separation energies plotted as deviations from the predictions of the semi-empirical mass formula,

$$M(Z,A) = Zm(^1H) + Nm_n - B(Z,A)/c^2.$$

where Z is the number of protons, m(^{1}H) is the atomic mass of hydrogen, N is the number of neutrons, m_n is the mass of the neutron, and B is the binding energy. The separation energy increases gradually with N or Z except for a few sharp drops that occur at the same neutron and proton numbers. The sharp drops are assumed to represent the filling of the major shells, and become known as "magic numbers". The nuclear potential is understood by assuming the motion of a single nucleon is governed by the collective potential of all the other nucleons. If nucleons are treated this way then the nucleons are allowed to occupy the

energy levels of a series of subshells. Definite spatial orbits depend on the Pauli principle. When nucleons collide they will transfer energy to each other, but if all of the energy levels are filled up to the shell gap, there is no way for the nucleons to gain energy other than by moving up to the valence level. The other levels near the original level would also be filled and would not be able to accept an additional nucleon. A transfer from a low-lying level to the valence band would require more energy than the nucleons are able to transfer in a collision. Therefore the nucleons can be treated as transparent to one another, which allows for spatial nucleon orbits.

2.3 Developing the Shell Model

The first step in developing the nuclear shell model is figuring out the potential. First, the 3-dimensional Schrodinger equation is solved for both an infinite square well and a harmonic oscillator. When solved the degeneracy of each level is proportional to the number of nucleons that can be put into each level, or $2(2\ell + 1)$. The factor $(2\ell + 1)$ comes from the m_ℓ degeneracy and the extra factor of 2 comes from the m_s degeneracy. Analagous to atomic physics, spectroscopic notation is used to label the levels. The main difference in the nuclear spectroscopic notation is that n is used to count the number of levels with a given l value. The levels derived from the infinite square well and harmonic oscillator potentials can be seen in Fig. 2.2 adapted from Ref. [19]. The magic numbers start off agreeing (through 20) but after that agreement with observed magic numbers disappears.

Improving the model further, starts with finding a more realistic nuclear potential. The previously mentioned potentials fail due to a need for infinite proton-neutron separation energies, and the inability for them to get the correct magic numbers. The potential,

$$V(r) = \frac{-V_o}{1 + exp[(r - R)/a]},$$

was chosen. The depth of $V_o = 50$ MeV is chosen to ensure the proper separation energies, and $R = 1.25A^{\frac{1}{3}}$ fm and $a = 0.524$ fm are the mean radius and skin thickness respectively. The resulting energy levels can be seen in Fig. 2.3 adapted from Ref. [19]. When compared to the harmonic oscillator and infinite square well potentials, the ℓ degeneracies disappear but the splitting becomes more apparent as the energy increases, and eventually the spacing becomes as drastic as the harmonic oscillator. The proper magic numbers still were not achieved. It would take another borrowed concept from atomic theory to satisfy this remaining issue.

The spin-orbit interaction in atomic physics causes the observed fine structure of spectral lines. This comes from the electromagnetic interaction of the electron's magnetic moment with the magnetic field created by the motion about the nucleus. While this force would not be great enough to effect the structure of the nucleus, the idea of of a nuclear spin-orbit force that is not electromagnetic in origin was adopted. In 1949, Mayer and Jensen successfully applied the nuclear spin-orbit interaction to the nuclear potential, resulting in the proper subshells.

The spin-orbit interaction is represented as $V_{so}(r)\ell\cdot$ s, where the $\ell\cdot$ s part allows for the reordering of the levels and referring to the total angular momentum as $\mathbf{j}= \ell \ +$ s. The spin of a nucleon is $\frac{1}{2}$, and therefore,

$$\mathbf{j} = \ell \pm \frac{1}{2}.$$

(except when $\ell = 0$, then only j=$\frac{1}{2}$ is allowed). The expectation value of $\ell \cdot \mathbf{s}$ can be found to be,

$$\ell \cdot \mathbf{s} = \frac{1}{2}[j(j+1) - \ell(\ell+1) - s(s+1))\hbar^2.$$

2.4 USD,USDA,USDB

The USD Hamiltonian was first developed by [2] and provided realistic *sd*-shell wave functions for nuclei in the valley of stability. As one ventures into the realm of unstable nuclei, the USD Hamiltonian needs some adjusting.

The USD Hamiltonian is defined by 63 *sd*-shell two-body matrix elements (TBME) and three single-particle energies [2] and can be seen in Fig. 2.4 of [8]. The values come from the renormalized G matrix with modifications to reproduce the experimental binding energies and excitation energies for nuclei in the region A = 16-40. The new fits to the USD Hamiltonian, USDA and USDB, are based on an updated set of binding energies and energy levels [20].

The original USD Hamiltonian was made from a least-squares fit of 380 energy data with experimental errors of 0.2 MeV or less. The rms deviation from data and theory was about 150 keV. Since the 1980's much more information on neutron-rich nuclei has been discovered, allowing for more accurate fitting and a more complete set of low-lying energy levels for *sd*-shell nuclei. Also, computing power has significantly increased, allowing calculations to be done in a matter of hours, as opposed to days. Therefore, [20] refined the USD Hamiltonian

with 608 energy data in 77 nuclei distributed over the *sd*-shell. The new Hamiltonians, USDA and USDB, allow for a new level of precision for realistic shell-model wave functions.

The data for the fits were obtained from [21] and a few more recent sources [5,17] for A= 21-40 nuclei. The ground-state binding energies were taken from the 2003 mass evaluation of Audi, Wapstra, and Thibault [22].

The binding energies were found relative to ^{16}O using the Coulomb energy correction used for USD [23],

$$BE(A,Z)^r = BE(A,Z) - BE(^{16}O) - E_c(Z).$$

The Coulomb energy corrections were obtained from energy differences of isobaric analog states for nuclear near N=Z.

The new Hamiltonian was developed using 608 states in 77 nuclei. The distribution of these states over the *sd*-shell nuclei is shown in Fig. 2.5 of [8]. Most of the new data was added in the middle of the *sd*-shell and for neutron-rich nuclei.

The effective Hamiltonian was described based on the work of Chung and Wildenthal [2, 23] as the sum of one and two body operators for the *pf*-shell. This Hamiltonian is comprised of a number operator for the spherical orbits, and a scalar term, the two-body density operator for nucleon pairs in various orbits coupled to spin quantum numbers J M and isospin quantum numbers T T_z.

The calculations for the wave functions, energies, occupation numbers, and scalar two-body transition densities were done using OXBASH [8]. This calculation took about 12 hours on a desktop PC. The data set included ground-state binding energies and all positive parity energy levels for *sd*-shell nuclei. In addition, levels above the energy where one level has an unknown J^π were excluded. This usually occurred between 5-7 MeV. Also, the ground and excited states that occur in the region where the experimental level density is much greater than the theoretical level density were left out. This region occurs at N= 19-20 and Z = 10-12 and this is known as the island of inversion.

With these exceptions, 608 states in 77 nuclei were examined with errors of less than 0.2 MeV. The single particle energies are taken to be mass independent as was done in USD. The reason they can be considered mass independent is because mass dependence has very little effect on the rms values since it can be compensated by the two-body matrix elements. The effective single particle energies are defined by the introduction of the monopole linear

combinations of the TBME [8] to the original SPE. The effective SPE are described well by data, however the original SPE and monopole TBME cannot be divided based solely on the *sd*-shell data.

Mass dependence is then introduced into the two-body matrix elements. This mass dependence accounts for what would be expected from a medium-range interaction with the harmonic-oscillator radial wave functions. The linear combinations of the Hamiltonian parameters were constrained to the values obtained from the renormalized G matrix applied to the *sd*-shell (RGSD). These calculations were based on a Bonn-A N N potential and can the TBME can be seen in Table 20 of [24].

The USD Hamiltonian was used for the first interaction. Then the equations were iterated for 30 well determined and varied linear combinations and 36 less well determined linear combinations set to the RGSD values. This iteration was continued until the energies had converged to a the level of about 10 keV. This constrained Hamiltonian is known as USDA.

As can be seen in Fig. 2.6 of [8] a plateau in the rms deviation of about 170 keV between 30-45 linear combinations occurs, followed by a gradual drop until 56 linear combinations with rms deviation of 130 keV that does not decrease much further all the way out to 66 combinations. For this reason, another Hamiltonian called USDB was developed varying 56 linear combinations of the parameters. More specific information on the parameters used for the development of USDA and USDB can be seen in [8].

Therefore, two new Hamiltonians have been developed to described *sd*-shell nuclei. A more conservative Hamiltonian, USDA, that is closest to the RGSD and gives a good but not best fit to the data, and USDB while differing more from the RGSD but giving a better fit to the data. Both USDA and USDB (and USD) were compared to the current work, giving an early comparison of USDA and USDB for neutron rich experimental data.

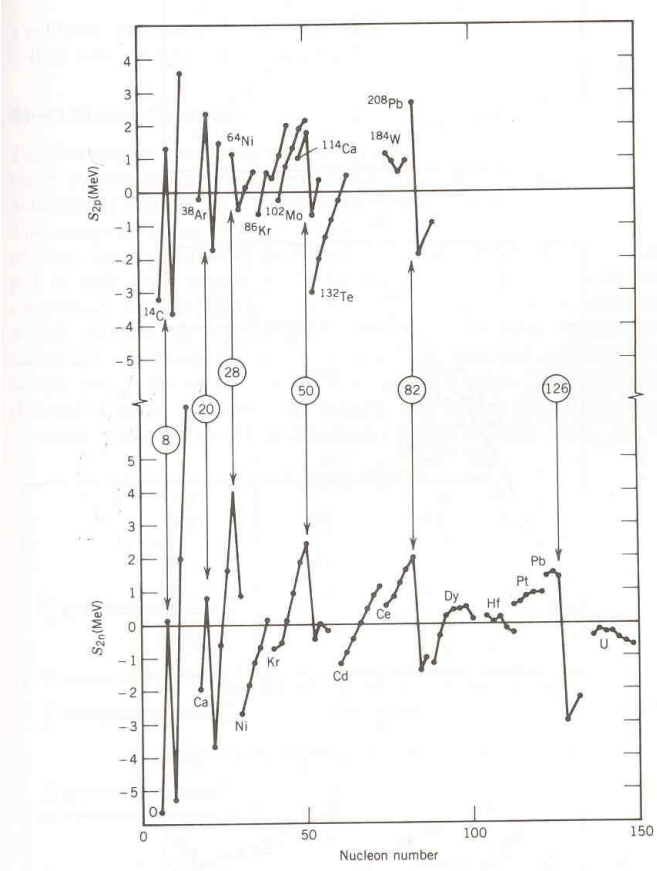

Figure 2.1: The top portion of the plot is the two-proton separation energies of a sequence of isotones. The bottom portion is a plot of the two-neutron separation energies of sequences of isotones. The magic-numbers reveal themselves through the apparent sharp changes. The plotted information are the measured values and the predictions of the semi-empirical mass formula. The measured values are from 1977 atomic mass tables (A.H. Wapstra and K. Bos, *Atomic Data and Nuclear Data Tables***19**, 215 (1977)).

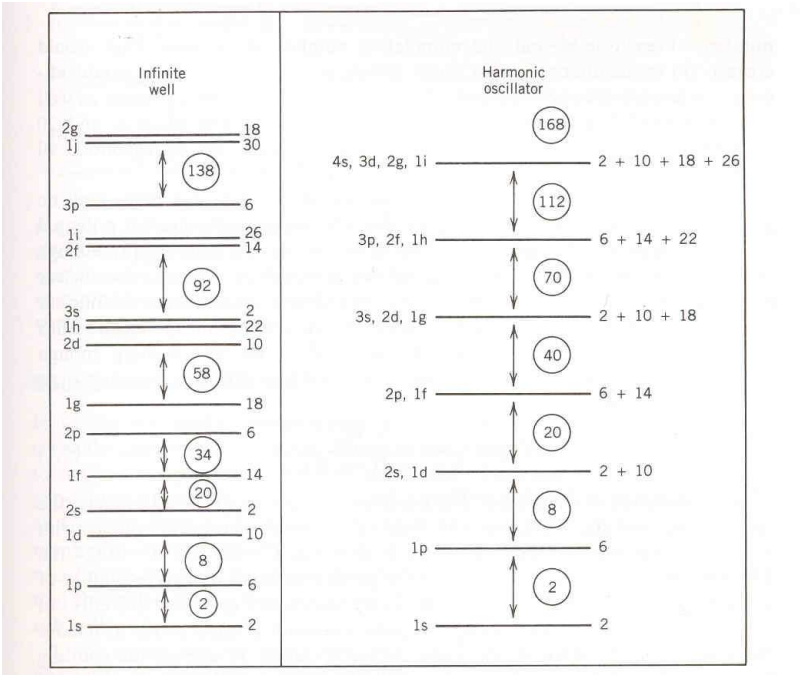

Figure 2.2: Shell structure obtained from solving infinite square well and harmonic oscillator potentials.

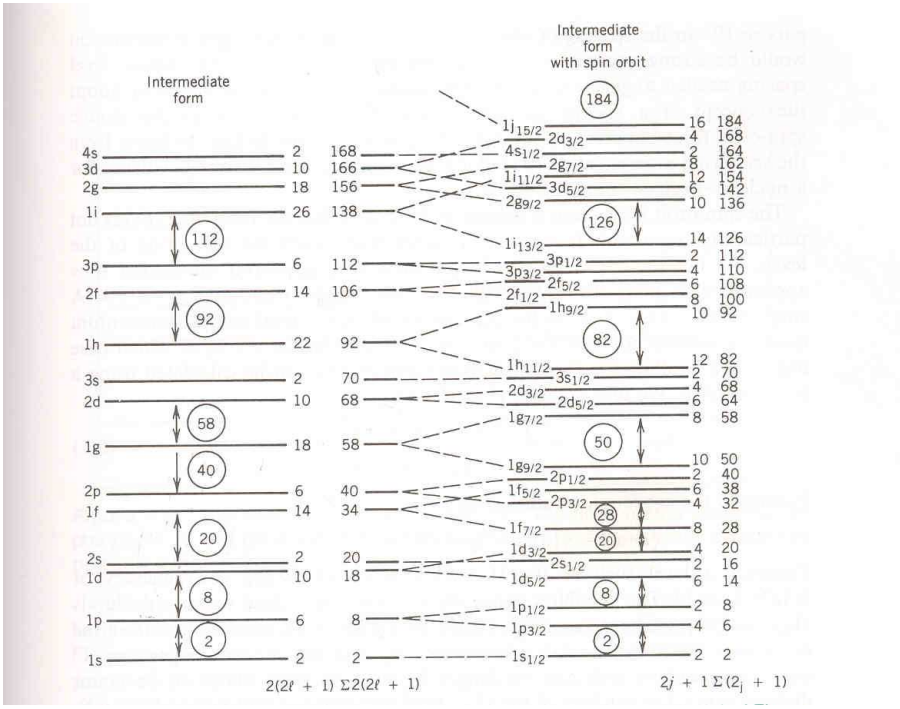

Figure 2.3: The information at the left is the energy levels calculated with the modified potential. To the right is the total number of nucleons up to that level. The far right side of the figure shows the effect of the spin-orbit interaction, which splits the levels for $\ell > 0$ into two new levels.

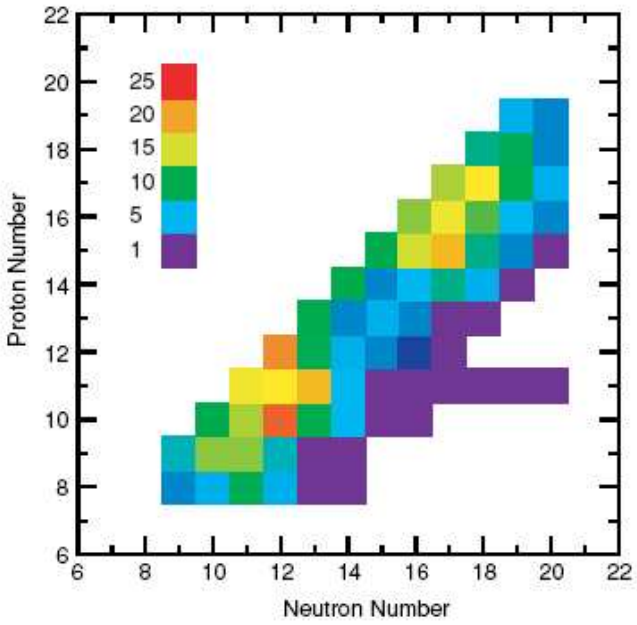

Figure 2.4: Number of states used for the USD Hamiltonian for each nucleus

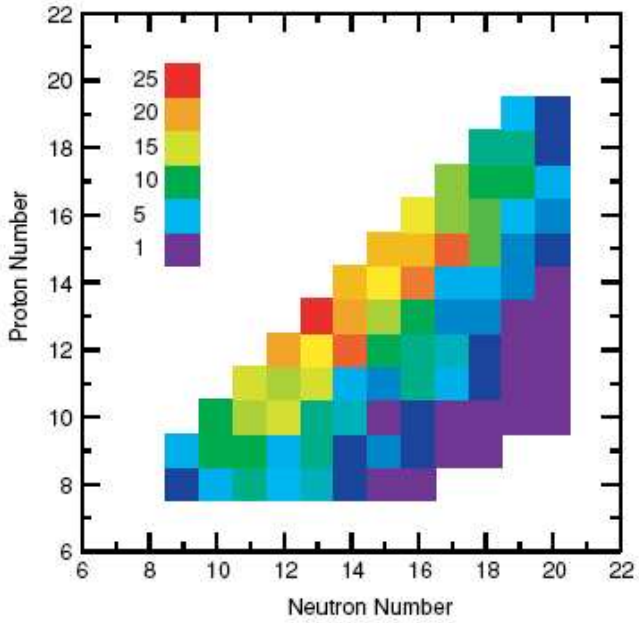

Figure 2.5: Number of states used for the USDA and USDB Hamiltonians for each nucleus

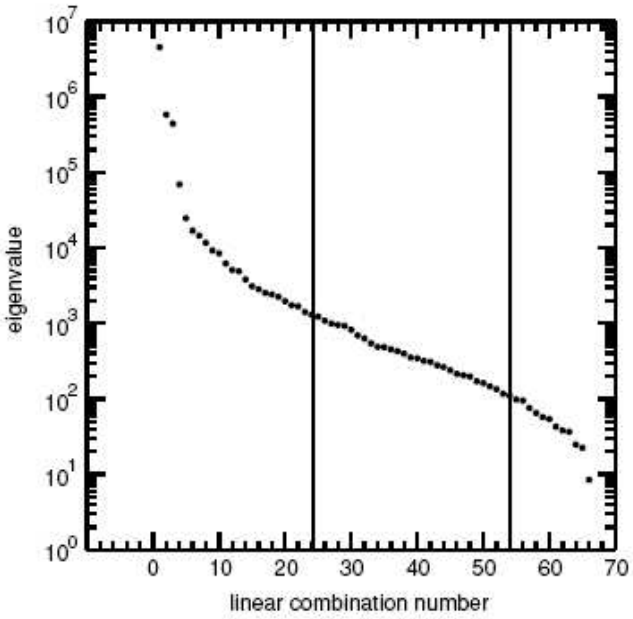

Figure 2.6: Eigenvalues D_i of the fit matrix.

CHAPTER 3

Experimental Details

3.1 Radiation and its Detection

3.1.1 Types of Decays

In the early days of radioactive study, Ernest Rutherford identified three different types of decay. He named them α, β, and γ. In α and β decay, an unstable nucleus emits an α or β to become a more stable nucleus of a different nuclear species. In γ decay, an excited state decays towards the ground state through the emission of a γ ray, without changing the nuclear species. Alpha decay will only be briefly discussed as it was not investigated in this dissertation. However, more detailed information on the processes of β and γ decay will be discussed in later sections.

Alpha decay occurs when a nucleus emits an α particle in an attempt to reach a more stable nucleus. Rutherford and his co-workers were the first to recognize the alpha particle as the $^4\mathrm{He}_2$ nucleus. It is a tightly bound system, and therefore the kinetic energy released in the decay is maximized. The decay process is

$$ {}^{A}_{Z}X_{N} \rightarrow {}^{A-4}_{Z-2}X'_{N-2} + {}^{4}_{2}He_{2} $$

where X and X' represent the chemical symbols of the initial and final nuclei. Notice that the number of protons and the number of neutrons must separately be conserved in the decay process. Alpha decay is typically favored for heavy nuclei.

The most basic β decay process is the conversion of a proton into a neutron or a neutron into a proton. In a nucleus, β decay changes N and Z by one such that, Z $\rightarrow$ Z$\pm$ 1, N $\rightarrow$ N$\mp$1, and A = Z + N remains constant. It can be said then that β decay offers an unstable nucleus a really convenient way to become a stable isobar. There are three different versions of beta decay. Negative β decay where the β is an ordinary electron and represented by β^-,

$n \rightarrow p + \beta^- + \nu_e$ (this is also the type of β decay to be discussed in this dissertation), positive β decay, where $p \rightarrow n + \beta^+ + \overline{\nu}_e$, and orbital electron capture $p + e^- \rightarrow n + \overline{\nu_e}$.

An emission of a γ ray occurs when an excited state decays to a lower excited state or ground state. This gamma ray will have energy equal to the energy difference between the excited and lower or ground nuclear states. Gamma emission is observed for nuclei with A ≥ 5, ie nuclei with excited bound states, and can follow alpha emission, or in the case of this dissertation, beta-decay (which often leads to excited states in the daughter nucleus). The half-lives due to γ decay are usually less than 10^{-9}s, but occasionally there are longer lived γ decays, known as isomers.

3.1.2 Radiation

γ rays are detected through their interaction with the detector material. There are three major interaction processes resulting in energy transfer that need to be addressed when effectively detecting γ rays: the photoelectric effect, Compton scattering, and pair production.

The photoelectric effect was used to demonstrate the quantum nature of light by Einstein in 1905. This effect is favored for low-energy γ rays. The photoelectric effect occurs from the interaction of a γ ray with a tightly bound atomic electron. The energy of the γ is transfered to the electron emitted from the atom with an energy of

$$E_e = h\nu - E_b, \tag{3.1}$$

where hν is the absorbed photon energy and E_b is the binding energy of the photoelectron in its original atomic shell. As the photoelectron is removed, a vacancy in the atomic orbital is produced which is then occupied by an electron from a higher orbital. This process results in the emission of an X ray, which is, in turn, absorbed by the material.

The probability of photoelectric absorption is found to vary with the atomic number, Z, of the detector material,

$$\tau \, \alpha \, Z^5. \tag{3.2}$$

Consequently, high Z materials are often used in X-ray and low-energy γ-ray shielding.

Compton scattering, Fig. 3.1, occurs between energies of 150 and 8000 keV, when an incident γ ray scatters off a loosely bound electron in the absorption material. A portion of

the γ ray's initial energy is imparted to the electron and can be described as,

$$E_e = \frac{E_\gamma}{(1 + E_\gamma[1 - cos\theta]/m_o c^2}, \tag{3.3}$$

where E_γ is energy of the incident γ ray; θ is the angle the scattered photon makes with the direction of the incident photon and $m_o c^2$ is the rest mass of the electron. As shown in Eq. 3 the maximum energy for the electron that can occur is when the γ ray is scattered backwards, i.e θ=180^o. However, no matter the angle, E_e is always less than E_γ, and less than 100% of the γ ray energy is absorbed by the detector. However, multiple scattering can occur which results in a wide variety of energies recorded by the detector.

Pair production happens at energies where $E_\gamma \geq 1022$ keV. In this process, a γ ray is converted to an electron-positron pair. This process is only significant for γ rays with energy greater than 1 MeV. The positron that is formed by this process is quickly converted into photons by its annihilation with another electron. These annihilations can have a large impact on the final γ spectrum, resulting in the presence of a very noticeable peak at 511 keV.

3.1.3 Detectors

Different materials can be used in the detection of radiation. The selection depends on the experimental requirements, such as timing, energy resolution, and the type of radiation being detected. In this section, germanium, silicon, and bismuth germanate are discussed, since these were used in experiments presented in this dissertation.

Semiconductor Detectors

A pure semiconductor has a filled valence band consisting of electrons that are bound to specific lattice sites and an empty conduction band where the electrons are free to move. These two bands are separated by a band gap which determines whether the material is an insulator or a conductor. If the band gap is large, $\geq$ 5 eV, the material is an insulator. However if the material has a small band gap on the order of 1 eV this material is known to be a semiconductor. At room temperature, electrons can be thermally excited across this gap into the conduction band, leaving behind a "hole". As an electron from a nearby atom fills this hole, in turn creating a new hole, the hole seems to migrate through the material.

To control the conduction in semiconductors, small amounts of dopants are added, which introduce new atoms into the lattice of the crystal, generally either group V or group III atoms. For dopants that belong to group V (P, As, Sb) four of the electrons form covalent bonds with the neighboring semiconductor material (either Si or Ge). This allows the fifth electron to move around the lattice and form a set of donor states below the conduction band. Since there is an excess of negative charge, this material is classified as a n-type semiconductor. If group III dopants are added and attempt to form covalent bonds with the neighboring atoms, holes are produced. These form acceptor states just above the valence band, which makes an excess of positive charge. These materials are classified as p-type semiconductors. See Fig. 3.2.

When p and n type materials are doped on either end of a strip of Si, the electrons from the n-type will diffuse across the junction into the p-type material and combine with the holes. In the region near the junction, the charge carriers are neutralized, leaving behind what is known as a depletion region. This process leaves behind fixed donor and acceptor sites in the n and p type regions respectively. The space charge from the fixed sites creates an electric field which eventually stops any more migration. This is known as the junction diode.

When radiation enters the depletion region and creates electron-hole pairs, electrons can flow in one direction, and holes in the other, and then the total number of electrons collected can form an electronic pulse whose amplitude is proportional to the energy of the deposited radiation.

Si Surface Barrier Detectors

As described in the earlier section, p and n type semiconductors are brought together and combined with the presence of an internal electric field to make a system where radiation is transformed into an electrical pulse that can be measured. Si surface barrier detectors have their p-n junction reversed biased to create an external electric field that will carry electrons away from the depletion region very quickly ($\leq$ 10ns). This reverse biasing is done by applying a negative voltage to the p-side of the junction and electrons located in the p-side travel across the barrier to the n-side of the depletion region. Similarly a positive voltage is applied to the n-side of the junction to deal with the holes. This results in a very low leakage current since the number of holes in the n-side and the number of electrons in

the p-side will be relatively small, which allows for the detection of electrical signals from the interacting radiation. Si surface barrier detectors are produced by exposing a p-type crystal to a vapor of n-type impurities, such as P. An electrical contact is created by etching the surface and evaporating a thin gold layer onto it (an n-type material such as Al can also be used). Only the depletion region is sensitive to incoming radiation, but to get to the depletion region, radiation must often pass through a non-interacting layer called the dead layer. Surface barrier detectors have very small dead layers since the thickness of the evaporated material is kept extremely thin.

HPGe Detectors

The other commonly used type of semiconductor material is Ge, which is the preferred choice for γ ray spectroscopy due to its high electron density. Germanium is also kept at reverse bias, but at a much higher voltage than their Si counterparts (up to 4 KV). High purity Germanium is used since since they have impurity levels as low as 10^9 atoms/cm^3, compared with 10^{12} atoms/cm^3 for normal semiconductors. However there can be small residual impurities remaining in the Ge that can make it slightly p-type or slightly n-type depending on the type of impurities present.

To use HPGe for γ-ray spectroscopy, a large volume of Ge is needed. The detectors are constructed in a coaxial shape (Fig. 3.3). Electrical contacts are at the center and outside of the crystal. For n-type detectors, the inner contact is a thick n^+ (the "+" sign refers to a highly doped material)contact that is approximately 600 μm thick, and the outer contact is a thin p^+ contact on the order of 0.3 μm thick.

Electron-hole pairs are formed at an energy close to 3 eV in HPGe, which means that many pairs can be formed and many charge carriers are released in each γ ray interaction. This results in small statistical fluctuations in the the number of charge carriers per pulse and therefore there is a good signal to noise ratio. Due to a small band gap, electrons from the valence band can be thermally excited quite easily over the gap to the conduction band. The excess thermal noise is quenched by cooling the detectors to 77 K with liquid nitrogen.

Scintillators and BGO Suppression Shields

As described before, there are three ways a photon can interact with a Ge crystal. The photo-electric effect occurs when the entire photon energy is transfered to an electron in the

Ge crystal. Compton scattering occurs when the photon is scattered off an electron and transfers only a fraction of its initial energy. Pair production occurs when the energy of the incoming photon is greater than 1022 keV, and a positron-electron pair can be created. After the positron loses the majority of its energy it annihilates with an electron and emits two 511 keVγ rays. These γ's are absorbed by the Ge and then can either go through Compton scattering or the photoelectric effect.

When studying nuclear structure at the γ ray energy range of interest, Compton scattering is the dominant interaction. When γ's come into the HPGe and Compton scatter within the material it is very easy for these photons to scatter out of the detector. When this happens the energy imparted to the electron contributes to background in the γ spectrum, which limits the ability to decipher weak γ rays. Scintillators are used in conjunction with the HPGe to reduce background.

Incident radiation enters the scintillator material and undergoes a large number of interactions which raise the atoms to excited states. The excited states emit visible light which strikes a photosensitive surface, emitting one photoelectron per photon. These photoelectrons are multiplied and accelerated and formed into an output pulse by a photomultiplier tube (PMT).

There are a variety of materials used for scintillators and PMT's. The determination of which material to use is based on the application of use, the fraction of the incident energy that appears as light (light output), the efficiency (the probability for radiation to be absorbed), timing, and energy resolution. The first scintillating material was NaI and is still the most commonly used. In the case of NaI the valence band is full and the conduction band is empty (i.e. its an insulator). The incoming radiation excites electrons from the valence band into the conduction band across an energy gap of about 4 eV. The electron loses energy by emitting a photon and drops back into the valence band.

To increase the probability for photon emission small amounts of impurities called activators are added to the crystal. A commonly used activator is thallium(Tl). The activator provides states in the energy gap and allows for light emission to take place between the activator states.

Another material frequently used for scintillators is Bismuth Germanate (BGO). BGO is a pure inorganic scintillator that does not require an activator. Because Bi has a large Z (Z = 83) and the material has a high density, it is an ideal choice for γ-ray detection. The

absorption length, which is the amount of material required to absorb (1-$\frac{1}{e}$) of the photons entering the material, is 6 cm for BGO. However, BGO has a lower light yield in comparison to NaI. Therefore BGO is generally used in experiments where high γ-ray counting efficiency is more important than energy resolution.

FSU Compton Suppressed Detector Array

The FSU Compton Suppressed γ-Detector array consists of three Clover detectors comprised of four HPGe crystals each, nine single-crystal HPGe detectors and a low-energy HPGe photon spectrometer. The detectors can be mounted at many angles relative to the beam axis. Each HPGe is shielded with a BGO suppression shield to veto Compton scattered events.

γ-ray energy information is obtained through a series of electronics. A linear amplifier (AMP) with a shaping time of 3 μs is connected to an analogue to digital converter (ADC). A timing filter amplifier (TFA) is used to get the appropriate pulse shape for precise timing measurements, which integrates and differentiates the signals for a short period of time (200 and 20 ns respectively) depending on the noise level. The constant fraction discriminator (CFD) is used to generate a logic pulse that indicates the time of arrival of each pulse. The signals from the CFD's are then sent to the Blue Box which contains the timing and logic circuits used for coincidence and Compton suppression requirements. When an event is accepted by the Blue Box, a logic pulse is sent the ADC that digitizes the pulse. The ADC is interfaced with the data acquisition system through a CAMAC crate. A diagram of the electronics can be seen in Fig. 3.4.

An E-ΔE particle telescope can be used in conjunction with the HPGe array, and was used for the in-beam experiment presented in this dissertation. This telescope consists of four annularly segmented Si surface barrier detectors (only three were functional at the time of the experiment) mounted at 0^o relative to the beam, situated behind the target position. The ΔE detector was 150 μm thick, and the other three silicon detectors used for the E detectors were 1500 μm thick. These four detectors are combined to form the particle telescope. Energy loss measurements are taken with this telescope which allow for particle identification. The particle telescope is sensitive to the particle's mass, m, and proton number, Z.

The FSU HPGe Compton suppressed array and one of the Si surface barrier detectors

can be seen in Fig's 3.5 and 3.6.

3.2 Experimental Details

Excited states in ^{30,31}Al were produced in similar and different ways. ^{30}Al was studied using two complementary approaches: the beta decay of ^{30}Mg and an in-beam experiment, while ^{31}Al was studied only by the beta-decay of ^{31}Mg.

3.2.1 Beta Decay

The parent nuclei ^{30,31}Mg were produced by intermediate energy projectile fragmentation at the National Superconducting Cyclotron Laboratory (NSCL) at Michigan State University. A primary beam of ^{48}Ca was accelerated to 140 MeV/nucleon using the Coupled Cyclotron Facility; the K500 was used to accelerate the $^{48}Ca^{8+}$ to 12.3 MeV/nucleon , which was injected into the K1200 to get the desired 140 MeV/Nucleon $^{48}Ca^{20+}$ beam. The maximum beam current was 15 pnA. The primary beam was fragmented in a 700 mg/cm^2 thick Be target located at the object position of the A1900 fragment separator (Fig.3.7) to obtain the nuclei of interest. A 300 mg/cm^2 wedge-shaped Al degrader was used at the intermediate image of the A1900 to disperse the fragments according to their M/Z ratios. Two different settings of the magnetic fields of the A1900 were used to obtain the two different Mg isotopes: Bρ_1 = 4.35 Tm, B ρ_2 = 4.21 Tm with 1% momentum acceptance for ^{30}Mg, and Bρ_1 = 4.52 Tm, Bρ_2 = 4.39 Tm with momentum acceptance of 1% for ^{31}Mg. A "cocktail" secondary beam consisting of F, Ne, Na, and Mg isotopes was selected at each A1900 setting.

The fully stripped fragments were implanted in a Double Sided Si microstrip Detector (DSSD), which forms a part of the NSCL beta-counting system (BCS) [25]. The DSSD is a single 4 cm x 4 cm silicon wafer whose electrodes are segmented in 40 1-mm wide strips in both the x and y dimensions. A 10 mm thick Al degrader was placed before the DSSD to ensure complete implantation within the 985 μm thick DSSD. This thickness was used to ensure sufficient silicon for detection of the high energy β particles expected from the decay of nuclei far removed from the line of beta-stability. The DSSD was placed between two 5 cm x 5 cm x 500 μm Si PIN detectors. An additional 5 cm x 5 cm x 500 μm PIN diode was located downstream of these. The PIN detectors and the DSSD were mounted on an ISO-160 flange for easy coupling to the beam-line vacuum. Two 50 pin feedthroughs on this

flange are used to bring the DSSD signals to a grounding board placed immediately outside the vacuum chamber. The grounding board provides a common ground for each of the 80 output channels. Additional detectors, including a parallel-plate avalanche counter and a 5 cm x 5 cm x 500 μm PIN detector, were located upstream of this array to provide beam diagnostics and energy loss information necessary for particle identification. The detector arrangement is shown in Fig. 3.8.

The electronics for the BCS are chosen to account for the range of charged particle energies that must be measured. A fast fragment implant will deposit more than 1 GeV total energy in the DSSD, while an emitted beta will deposit less than 1 MeV. The broad range of energies observed for implants and decays is dealt with by processing the grounded DSSD signals by six 16-channel preamplifier modules.

Dual-output amplifiers (low gain and high gain) were used to read the DSSD strips. The low-gain signals (0.03 V/pC) were used for fast implantation energy and the high-gain signals (2 V/pC) used for the low-energy beta-decay. The discriminator outputs were combined to generate the master trigger for the data-acquisition system. Three of these modules were specified to have inverted output signals, and the other three non-inverted, so that the processed outputs from both the front and back sides of the DSSD share the same polarity. The outputs were designed to drive 50 Ohm inputs with amplitudes of $\pm$ 2V. The signal rise time from both the low and high gain outputs is 320 ns. As a result, the low gain signals, which provide the fast fragmentation energy information are sent directly to Phillips 7164H CAMAC and/or CAEN V785 VME analogue to digital converters (ADC's) with no further shaping. Since the high-gain signals carry information about the low-energy beta decay events, they require further processing. This is achieved using Pico Systems 16-channel shaper/discriminator modules in CAMAC. The shaper gains and discriminator threshold levels were set via computer control over the CAMAC bus. The shaper output of the Pico Systems module is sent directly to an ADC (either CAMAC or VME) while each discriminator output is combined in a logical OR gate to provide the master trigger. Individual discriminator signals are also sent to coincidence registers for zero suppressed readout of both sets of energy ADC's and to scalers for rate monitoring. An electronics diagram can be seen in Fig. 3.9.

The energy resolution of the system was measured using α particles from a ^{228}Th source. Individual strip resolutions were observed to be better than 80 keV Full Width at Half

Maximum (FWHM) at 8.78 MeV.

Data were written directly to disk. Each recorded event was tagged with an absolute time stamp generated by two EG&G RC014 free running clocks in CAMAC with a resolution of 30.5 μs. At the beginning of an experimental run, these clocks are reset to zero and started using the CAMAC control bus. The first clock reaches its 16-bit full scale in two seconds while the second operates as a slave to the first, incrementing only as the first reaches its full scale and subsequently resets itself. The clocks are read with every master trigger so that each event carries a time stamp relative to the start of the current run. Decay times were obtained by subtracting the time of the fragment implant from that of its associated beta.

For the fragments to be properly correlated it is necessary that a given implanted fragment beta decays before another fragment is implanted in the same DSSD pixel. For this reason, the fragment beam was defocused to illuminate as much of the DSSD as possible. This lengthened the average time between implants within a given pixel by distributing implants over as many pixels as possible. Since the profile of the incoming beam is roughly Gaussian in both the horizontal and vertical directions, the beam spot is observed to be round while the detector itself is square. As a result, fragments are distributed over 1000-1200 of the 1600 DSSD pixels. To measure half-lives of range ≥ 1 s, the average time between implants was set to be greater than 10 s. This was achieved by maintaining an average implant rate of 100 Hz.

Fragments were unambiguously identified by a combination of multiple energy loss signals and time of flight. Fragment beta correlations were established in software as described above. A low-energy beta event was correlated to a high-energy implant event in the same or adjacent pixels of the DSSD. Light particles, transmitted with the secondary beam, were vetoed by a scintillator placed at the end of the BCS, increasing the fragment beta correlation efficiency. Fragment beta correlated particle identification spectra for the production of ^{30,31}Mg are shown in Figs. 3.10 and 3.11. The differences between the absolute time stamps of the correlated beta and implant events were histogrammed to generate a decay curve. To suppress background, implants were rejected if they were not directly followed by a beta event within a specified time period in the same or a neighboring pixel or if they were followed by a second implantation before beta decay. The time periods selected, based on the half-lives, were 5 s for both ^{30,31}Mg.

The β delayed gamma rays were detected using 12 detectors of the Segmented Germanium

Array (SeGA) [26] arranged around the BCS which can be seen in Fig. 3.12. The Ge detectors were energy and efficiency calibrated up to 3.5 MeV using standard calibration sources. The measured efficiency of the SeGA for this experiment was 5% for a 1 MeV photon. To take into account the extended nature of the γ rays, as the implants can decay anywhere in the detector, a simulation of the extended source geometry was performed using the Monte-Carlo n-particle (MCNP) code.

3.2.2 In Beam

Excited states in ^{30}Al were populated through the ^{18}O(^{14}C, pnγ) reaction at a beam energy of 22 MeV provided by the Florida State University Tandem Accelerator. The ^{18}O target with a thickness of 200 μg/cm^2 was made by anodizing Ta in an electrolytic cell with water enriched to 85% in ^{18}O on an 0.0127 mm thick Ta backing. The charged particles from the reaction were detected in the FSU E-ΔE silicon particle telescope. This telescope consisted of 3 annularly segmented silicon surface barrier detectors. A 150 μm thick silicon detector was used for the ΔE detector, and the two silicon detectors with thicknesses of 1500 μm each were combined to form the E detector.

Following the charged particle decay, the γ radiation was detected by the FSU Compton suppressed high-purity germanium (HPGe) detector array. At the time of this experiment, the array consisted of three four-crystal Clover detectors and six single crystal detectors. The three Clover detectors were located at 90^o from the beam axis along with two single crystal detectors. In addition, two single crystal detectors were each located at 35^o and 145^0 relative to the beam. The minimum trigger condition was a signal in one of the E detectors and another in a γ detector within the resolving time of about 70 ns. The data were written to disk during the experiment and later sorted into matrices for data analysis using GNUSCOPE [27]. In playback, the ^{30}Al events were selected by requiring the detection of a p or d in the particle telescope through gates drawn in the E-ΔE plane in coincidence with one or two γ rays. The dimensions of the particle-γ and particle-gated γ-γ matrices were 4000 x 4000, with a dispersion of 2 keV/channel. The matrices gated on p and d events were added together to combine both the p-n and d exit channels to improve the statistics. Angular distributions were measured by comparing the intensities of γ lines in the 90° detectors with those in the combined 135° and 45° detectors.

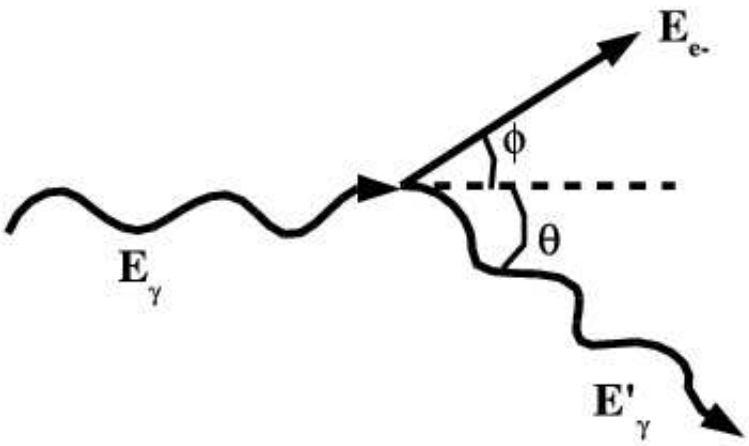

Figure 3.1: A diagram of Compton scattering

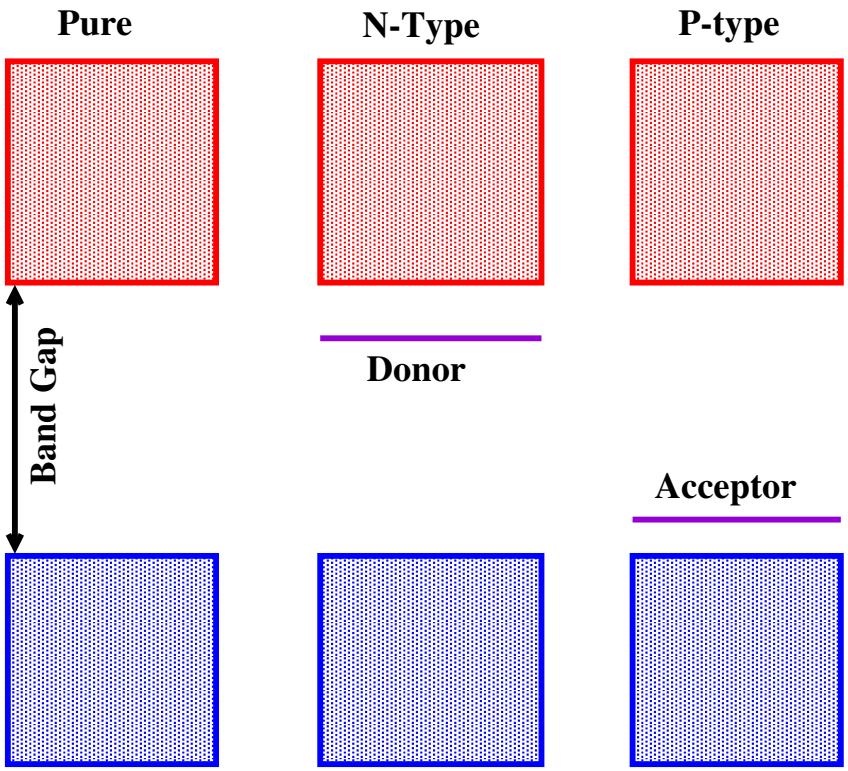

Figure 3.2: A diagram of p and n type semiconductors

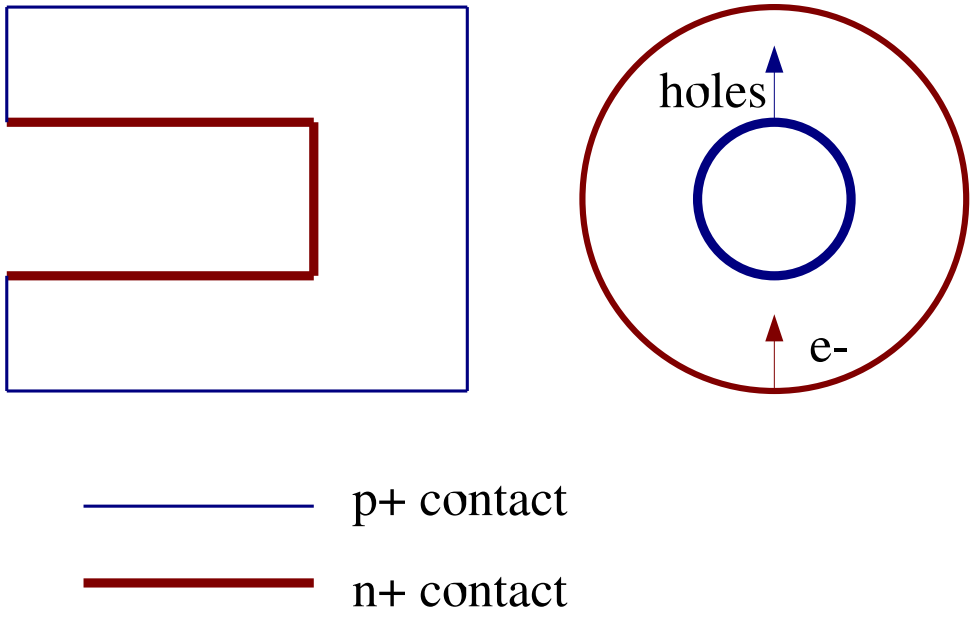

Figure 3.3: An internal view of an n-type HPGe crystal

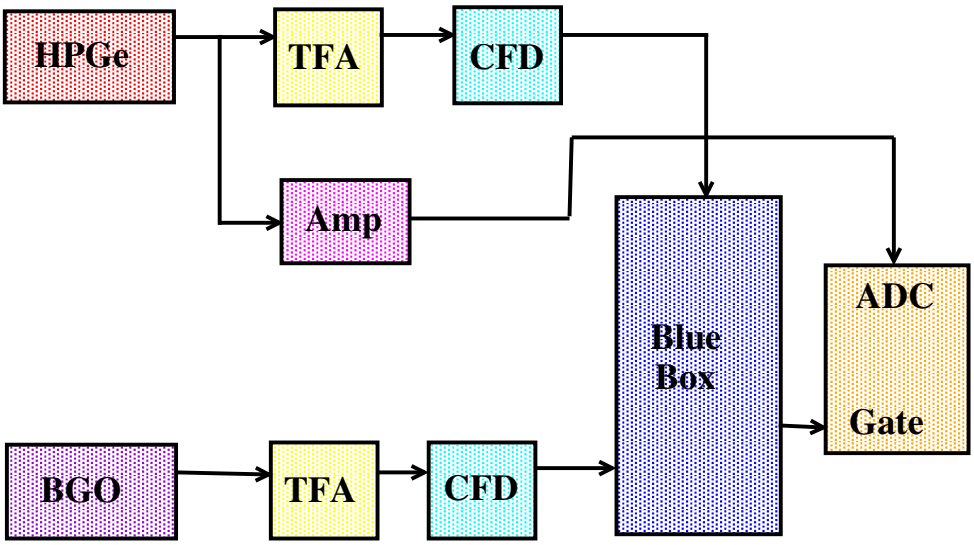

Figure 3.4: An electronics diagram for the HPGe with BGO suppression shield.

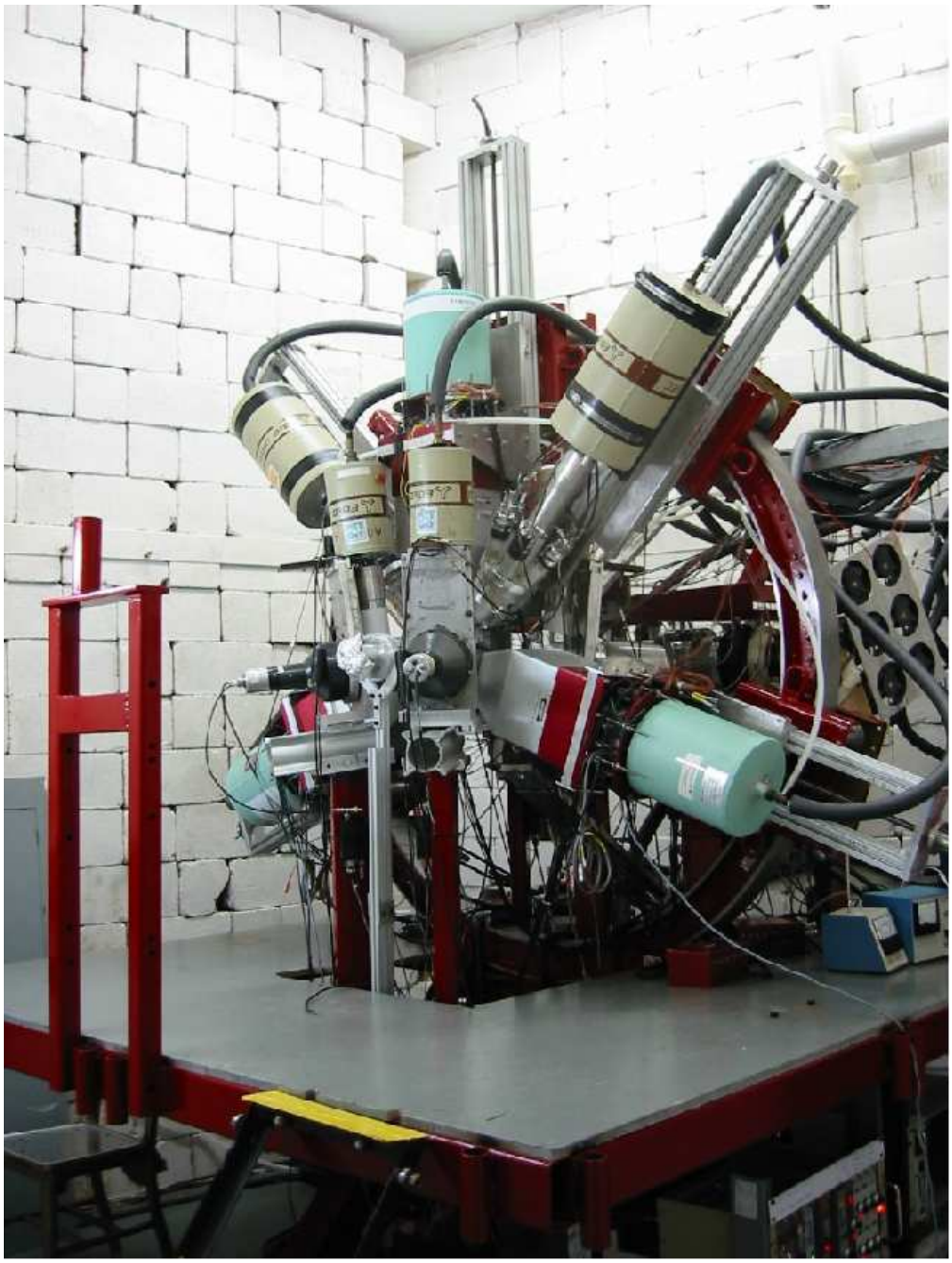

Figure 3.5: A photograph of the FSU Compton suppressed γ array

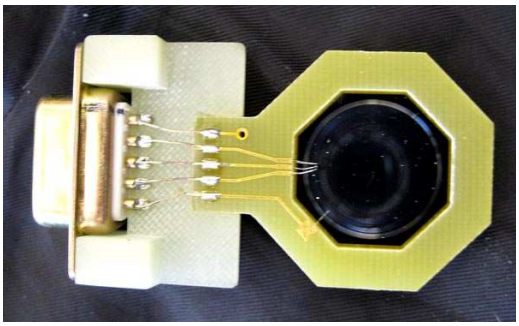

Figure 3.6: A photograph of the 150 μm thick silicon detector.

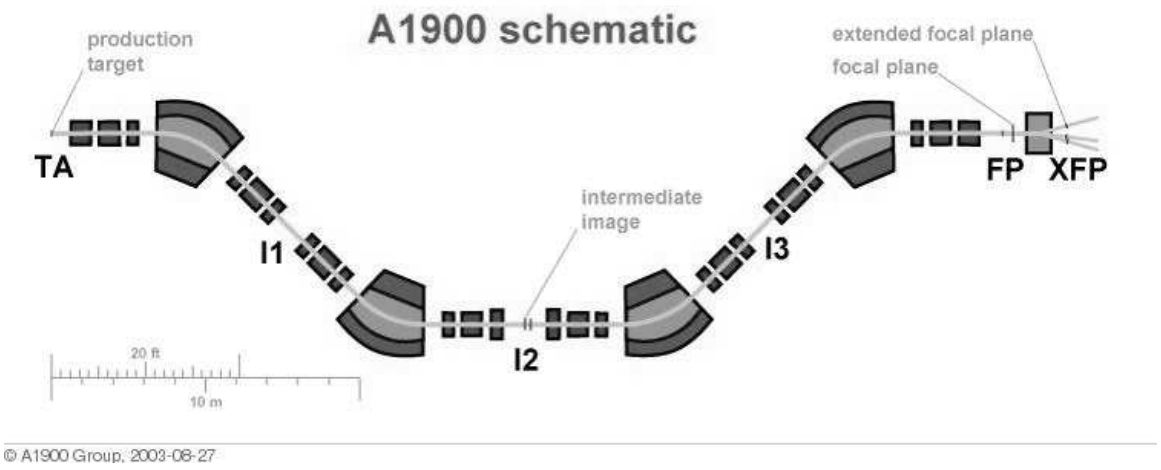

Figure 3.7: A Diagram of the A1900 fragment separator.

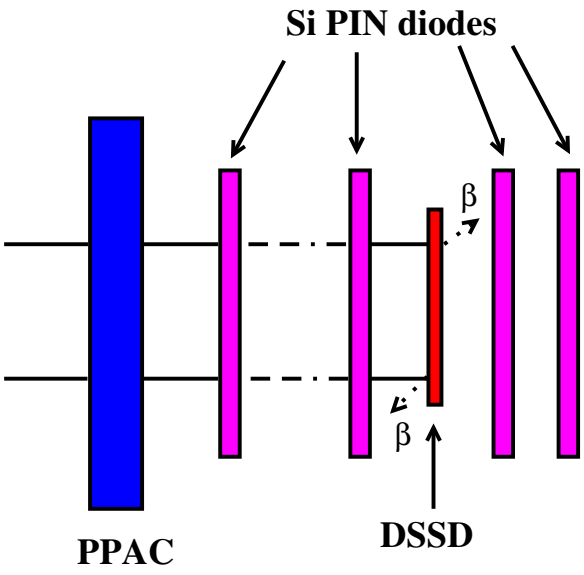

Figure 3.8: Arrangement of detectors in the BCS.

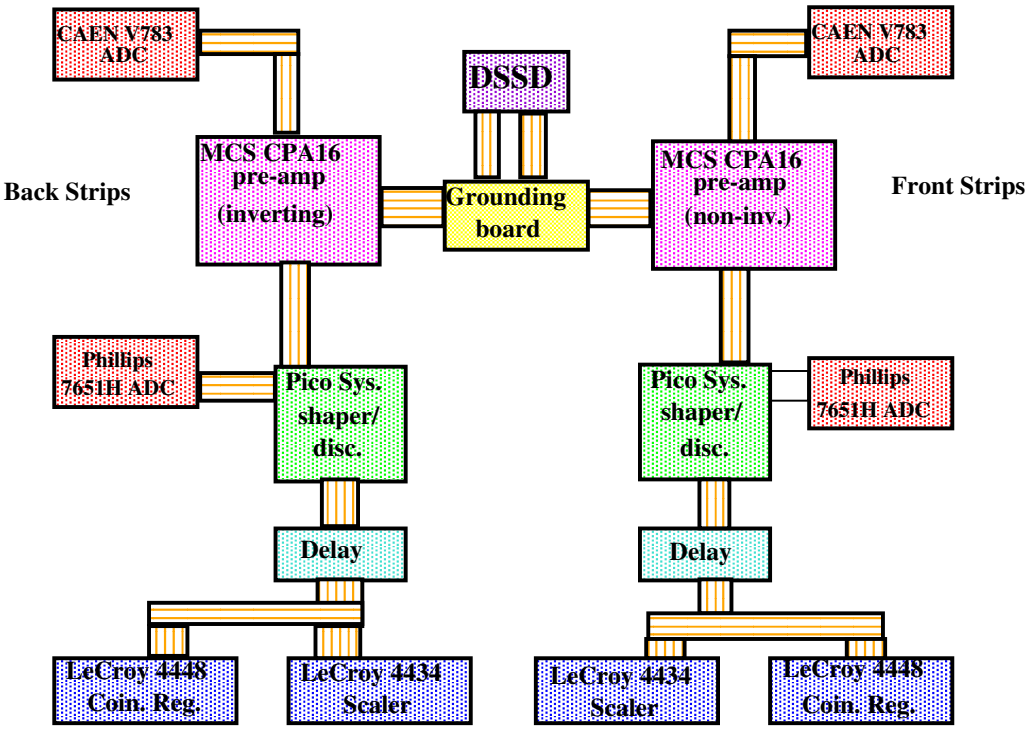

Figure 3.9: A diagram of the electronics for the BCS.

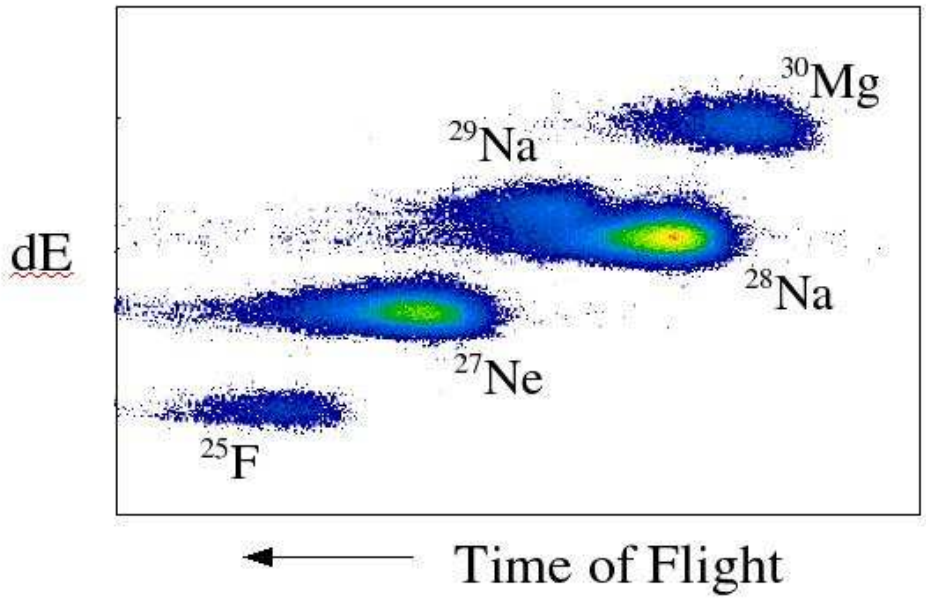

Figure 3.10: Two dimensional particle identification plot of time of flight vs. energy loss for implants that have a correlated β decay, observed with the A1900 setting optimized for the transmission of ^{30}Mg fragment.

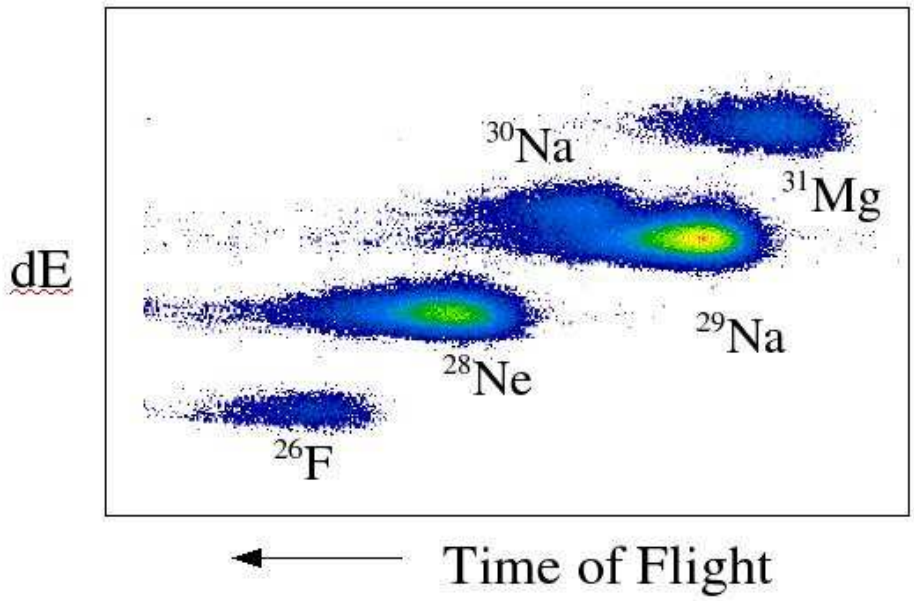

Figure 3.11: Two dimensional particle identification plot of time of flight vs. energy loss for implants that have a correlated β decay, observed with the A1900 setting optimized for the transmission of ^{31}Mg fragment

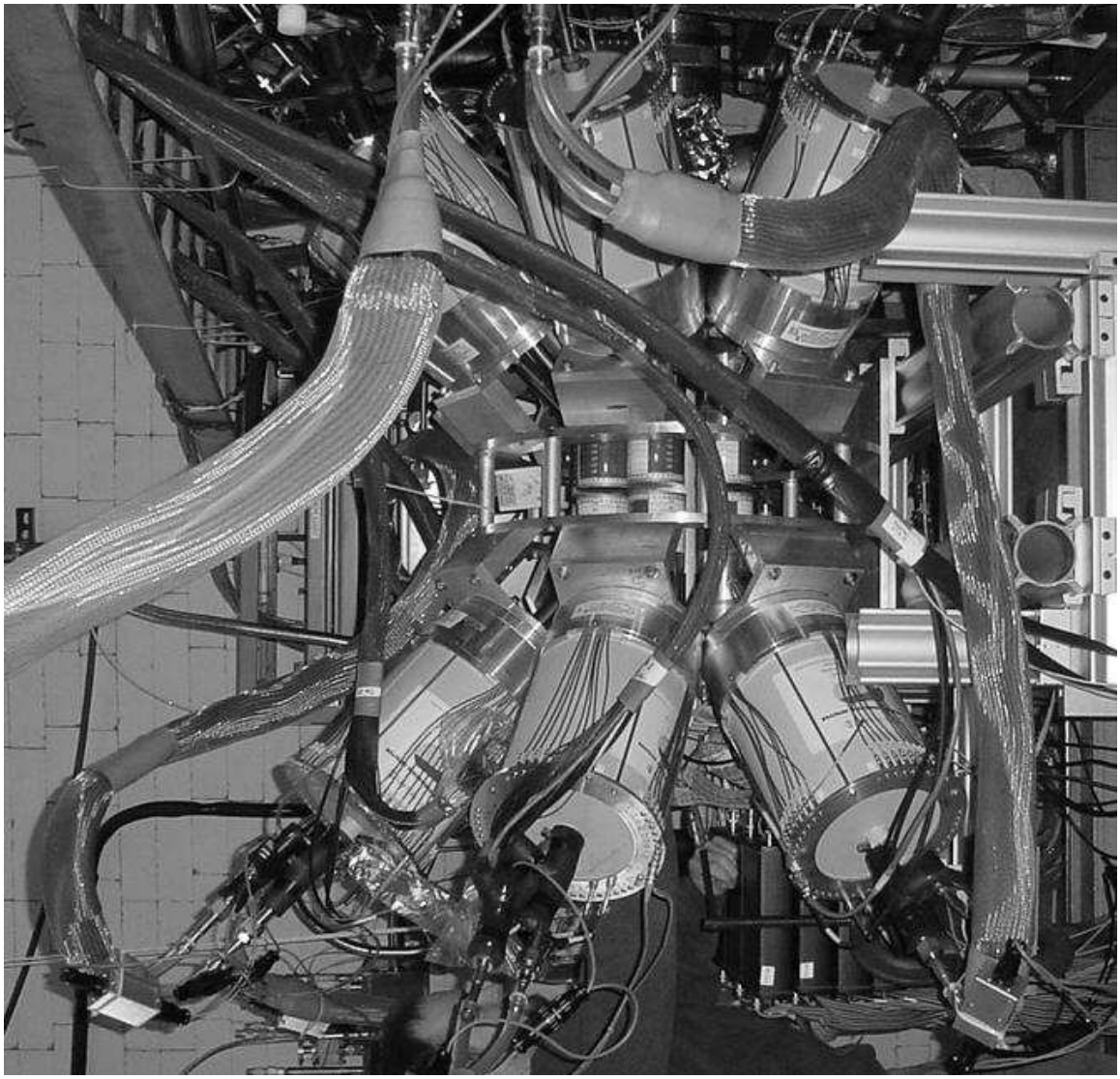

Figure 3.12: A photograph of the SeGA array

CHAPTER 4

Results for ^{30}Al

4.1 Results

4.1.1 Beta Decay

Half Life Measurement

The decay curve for ^{30}Mg was created by histogramming the time differences between the identified ^{30}Mg implants and β decay events in the same pixel for time intervals up to 10 s. The resulting decay curve is shown in Fig. 4.1 along with the fit based on the Bateman equations for the sequential decay of ^{30}Mg and ^{30}Al. The decay curve was constructed using 3 components, the decay of ^{30}Mg, the growth and decay of the daughter nucleus ^{30}Al, and the background. The decay constants of ^{30}Mg and the background were allowed to vary, as was the intial number of β decaying particles. The decay curve from β's correlated with γ rays of energy 244 keV or 444 keV was also fitted, as shown in Fig. 4.2. This fit was created using a 2 component exponential fit that included the parent decay and a long-lived background decay. Both decay constants for the parent and background decay were allowed to vary, as was the inital number of particles. The half-life obtained from the fragment-β correlated events was found to be 316 $\pm$ 5 ms, and that of the fragment-β-γ was calcuated to be 314 $\pm$ 7 ms. The average of these half-lives was used to determine the adopted half-life of ^{30}Mg. The value of 315 $\pm$ 6 ms is in good agreement with previous measurements of 325 $\pm$ 30 ms [13] and 340 $\pm$ 20 ms [28], and has higher precision.

Level Scheme

The β-delayed γ spectrum displayed 5 γ lines which represent transitions in ^{30}Al. Lines at 243, 443, 685, and 2165 keV have been previously reported for ^{30}Al, but the 2165 keV line was not placed in the level scheme [13]. A new 1725 keV transition was observed in this

study, which along with the 2170 keV line (2165 in Ref. [13]) leads to a new state at 2413 keV. The placement of all the lines in the present β-decay work is confirmed by the β-γ-γ coincidences shown in Figs. 4.3 and 4.4. The β-decay level scheme deduced from the present work is shown in Fig. 4.5. The energies and intensities of the γ lines following the β decays of ^{30}Mg are listed in Table 5.1. The nucleus in which the γ transition occurs is also listed.

The β-decay branching to each level in the daughter nucleus was calculated from the difference between γ-ray intensities feeding into and out of the level, using the measured SeGA efficiency and utilizing the initital number of β decaying particles derived from γ transitions populating the g.s. of ^{30}Si [21]. The possibility of β-delayed neutron decay was accounted for by measuring the branching to the first excited state in ^{29}Al, which was found to be approximately 2 percent and can be taken as a lower limit. The branching to the 244 keV state was approximately zero, suggesting that it is not populated by allowed β decay. The g.s. branch is also very small, which is consistent with the previously assigned spin and parity of 3^+. The apparent log ft values were deduced using the measured intensities for β decay, the measured half-life, and the Q_β values from the literature [22]. The apparent log ft values for the 688 keV and 2413 keV states are 3.8 ± 0.5 and 4.1 ± 0.4, respectively. These clearly represent allowed β-decay from the 0^+ g.s. of ^{30}Mg and confirm the previous 1^+ assignment to the former state [13] and provide a new 1^+ assignment to the latter.

4.1.2 In Beam

Analysis of data from the ^{18}O(^{14}C,pnγ)^{30}Al reaction yielded many new transitions not observed in β decay or previous work. These transitions were observed via p-γ-γ and d-γ-γ coincidences. Four of the previously known γ transitions and 13 new ones were observed. From these coincidences, the known 244 keV, 688 keV, 1120 keV, and 1246 keV states were confirmed. In addition, γ decays were observed from 6 states previously known only from the charge exchange experiments [11], and 4 new states were determined from their γ decays. The 991 keV γ transition reported in Ref. [15] from a proposed state at 991 keV was not seen in the present work. The particle-γ spectrum, Fig. 4.6, shows no evidence for a 991 keV transition. Coincidence spectra for various transitions in ^{30}Al are shown in Figs. 4.7, 4.8, 4.9, and 4.10.

The 1725 keV transition seen in the in-beam experiment must be different from the one seen in β decay because the former does not show coincidences with the 444 keV line (see Fig.

4.7) that appear in the later (Fig. 4.4). Coincidences between the 997 and 1605 keV lines (see Figs. 4.8 and 4.9) clearly establish a state at 5510 keV. The energy difference between the 3905 and 2298 keV states is 1607 keV, which is very close to that of the 5510→3905 keV transition. The possibility of a 1605-1607 keV doublet is also suggested by a possible peak around that energy in the 1605 keV gated coincidence spectrum (Fig. 4.9). The level scheme and the energies and intensities of the γ lines can be seen in Fig. 4.11 and Table 4.2, respectively.

4.2 DISCUSSION

The states observed in the present experiment are compared with those reported previously in Fig. 4.12. There is a clear one-to-one correspondence between the present work and the older charge-exchange results [11] up through the 2298 keV level. The differences in energy are well within the 15 to 20 keV uncertaintities reported for the charge exchange results. Above this, the 2413 (1^+ seen only in β decay), 2846, 4293, 5510, and 6422 keV states appear to have no counterparts reported in charge exchange. Counterparts were seen for the 2908, 3464, and 3905 keV levels.

4.2.1 Spins

The goodness of fit χ^2 between the measured and theoretically expected angular distribution for the 244 keV transition to the 3^+ ground state [13] is graphed as a function of mixing ratio δ for several possible spins of the 244 keV state in Fig. 4.13. Only a mixing ratio of $\delta = 0$ is possible for the spin-parity hypothesis of 1^+ and the fit is very poor at this point. The hypothesis of 3^+ would lead to $\delta \sim 0.62$ and an unreasonably large E2 admixture for such a low-energy transition. On the other hand, the hypothesis of 2^+ gives an excellent fit at $\delta = 0$ for pure M1 decay, which is expected for a low-energy transition. Thus, we assign 2^+ to the 244 keV state. This assignment is consistent with the non-observation of direct β feeding from the 0^+ g.s. of ^{30}Mg. The 2^+ assignment is also consistent with the tentative 1^+ or 2^+ in previous work [15, 11]. Fits to the angular distribution of the 444 keV line are shown in Fig. 4.13. In this case, the spin and parity of the 688 keV state have already been assigned 1^+, so several spin hypotheses are shown for the 244 keV state. J^π of 2^+ implies a nearly zero mixing ratio for the 444 keV transition, in agreement with the assignment based on the 244

keV angular distribution. Hypotheses of 1^+ or 3^+ imply substantial (and therefore unlikely) E2 components. Note that the existence of the 444 keV transition from a 1^+ state rules out any spin above 3 $\hbar$ for the 244 keV state.

Fits to the angular distribution of the 876 keV line (Fig. 4.13) rule out pure E2 decay and therefore, spins of 0^+ or 4^+, for the 1120 keV state. Possible spins of 1, 2, or 3 give good fits. The choice of 3^+ implies the smallest mixing ratio, but the possibility of significant E2 admixtures increases with the square of the transition energy and cannot be ruled out for the 876 keV decay. Spins of 2 or 3^+ were assigned to the 1120 keV state in the charge exchange experiment, with the former spin favored [11]. However, in a re-analysis of this data, only a spin of 3 was indicated in Fig. 3 of Ref. [12]. This is consistent with the preference for 3^+ in the present work. Fits to the 1246 keV transition (Fig. 4.13) favor spins of 2^+ or 4^+ for the 1246 keV state, with 4^+ giving a nearly zero mixing ratio. 1^+ and 3^+ are ruled out, but 5^+ is also possible. The fact that the 1246 keV state decays only to the 3^+ g.s. and not to the 2^+ or 1^+ states suggests a higher spin. Altogether, 4^+ is the most likely spin in the present analysis, followed by 5^+. This assignment is consistent with that from the charge exchange experiment [11].

No angular distributions were reported for the 1562 or 1802 keV states in the (t,^{3}He) reaction. It was also difficult to obtain reliable γ angular distributions for them in the current work. Both decay to the lowest 2^+ level, which limits their spin-parity to a range of 0^+ to 4^+ or 1^- to 3^-. The 2298 keV state was assigned J = 3 or 4 in the (t,^{3}He) reaction [12]. J=4 fits the angular distribution of its ground state decay with almost zero mixing ratio, while J=3 does not give a good fit (Fig. 4.14). Spin 4 also leads to a good fit at $\delta = 0$ for its 1178 keV decay branch. Spin 3 would imply a large mixing ratio which is less likely. The fact that it decays only to 3^+ states also favors spin 4. The 2846 keV state is placed based on the observed 1725-1120 and 1725-874-244 cascades.This state is newly observed, so no previous spin information is available. The angular distribution of the 1725 keV decay line is described well by spin hypotheses ranging from 1 to 4 for the 2846 keV level (Fig. 4.14).

The 2908 keV state was previously assigned spin 4 or 5 with unknown parity. The angular distribution of its 1662 keV decay line strongly favors a spin of 5 (Fig. 4.15). The angular distribution of its energetically unfavored 608 keV decay branch to another spin 4 state also favors spin 5 and esentially rules out 4 because of the very unlikely large mixing ratio (Fig. 4.15). The decay of the 3464 keV state to the lowest 4^+ level suggests higher spin and the

angular distribution of the 2217 keV γ ray also favors J=5 (Fig. 4.15).

The 3905 keV state was well described by 5^+ in Ref. [12]. The angular distribution of its 997 keV γ ray is described by a spin sequence of either $5 \rightarrow 4$ or $6 \rightarrow 5$ (Fig. 4.16) and not by a $\Delta J = 2$ or a $\Delta J = 0$ sequence. Since the 2908 keV state is much more likely to have spin 5, this would lead to an assignment of 6 for the 3905 keV state, in possible disagreement with the (t,^{3}He) result. However, no calculations for spins higher than 5 are shown in Ref. [12]. The decay of the 3905 keV state only to the lowest spin 5 level and not to any of the lower spin 4 states also makes the hypothesis of spin 6 more likely.

Neither the possible 4293, nor the 5510 or 6422 keV states, correspond to any previously reported levels. The angular distribution of the 2517 keV decay of the 6422 keV state is consistent only with Δ J = 1 (Fig. 4.16).

Note that the 6422 keV state lies about 700 keV above the neutron-decay threshold. Only the angular momentum barrier from a relatively high spin state would hinder neutron decay so much that γ decay predominates.

4.2.2 *sd* shell model and the positive-parity states

The USD Hamiltonian was adjusted to fit what was known of the structure of *sd* shell nuclei two decades ago [2, 20]. At that time, most of the available structure information was for nuclei in the valley of stability. Since then, a considerable amount of new structure information was measured experimentally for nuclei farther from the valley of stability, especially on the neutron-rich side. Recently, the Hamiltonian was adjusted again to reflect the wealth of new structure learned in the intervening years [8]. The USDA interaction was fitted by allowing 30 linear combinations of the two-body matrix elements to vary from the renormalized G matrix for the *sd* shell, whereas, for the USDB, 56 combinations were allowed to vary. RMS deviations of 170 (126) keV for the 608 energy levels fitted were observed for the USDA (USDB). The present work provides data not used in this fit for comparison with the three calculations in a nucleus with moderate neutron excess.

The *sd* shell model provides a good comparison for the positive-parity states with predominantly *sd* configurations. These calculations with all three interactions predict the same level ordering up through the lowest 4^+ state. There is also a one-to-one correspondence with the experimental levels (See Fig. 4.12), although the shell model energies tend to be somewhat lower. The RMS energy differences are 253, 187, and 191 keV for the USD, USDA,

and USDB interactions, respectively. Ie, the USDA and USDB give almost equally good fits to the level energies for the low-lying states, while the USD results are a little worse. This provides some support to the conclusion that the newer interactions are better adapted to neutron-rich nuclei.

The electromagnetic transition strengths provide a more detailed comparison between the calculations and experiment. They are shown in Table **??**. The theoretical branching ratios are based on the calculated B(M1) and B(E2) values (with effective charges of 1.5 and 0.5 for protons and neutrons, respectively) and the experimental transition energies. There is very good agreement in the branching ratios up through the lowest 4^+ state, which gives further confidence in the spin assignments given in Fig. 4.12.

Focusing on the lowest spin states, only one 1^+ state has been observed above 2 MeV, but all three calculations predict two 1^+ levels at about 2100 and 2500 keV. USD calculations [3] predict log ft values of 3.7, 4.1, and 6.8 for the 493, 2139, and 2538 keV levels. These are in good agreement with the experimental values if the 2413 keV state corresponds to the 2139 keV USD prediction. The very weak β branch implied by the large predicted log ft value for the 2538 keV level would explain why it was not observed experimentally. The predicted γ-decay branching ratios for the second theoretical 1^+ state also agree rather well with experiment, keeping in mind that weaker branches would not be observed experimentally.

It is unlikely that the 0^+ states were populated significantly in the ^{14}C + ^{18}O reaction since even the second 1^+ state was not observed. In the compilation [22], the 991 keV state is shown to decay only to the 1^+ state at 688 keV by a 303 keV γ ray. This would make it a candidate for the first predicted 0^+ state. However, no evidence for a 303 keV γ ray was found in the β-decay or in-beam data. The only published information on the purported 991 keV state is the observation of a ground-state decay [15]. As mentioned before, we see no evidence for this transition or state.

The comparison with theory becomes less clear above 1500 keV and spin 1. Based on their energies, the states observed at 1562 and 1802 keV are the best candidates for the predicted 2_2^+ and 2_3^+ levels. However, there is only limited agreement between the observed 100% decay branch of the 1562 keV state to the 244 keV level and the predicted branching ratios of 38% to 57% for the 2_2^+ state. There is essentially no agreement between the observed 100% $1802 \rightarrow 244$ keV decay and the 1% to 17% branches calculated for the 2_3^+ state, but partial agreement with the 28% to 51% branches calculated for the 2_4^+ state about 600 keV higher in

energy than the 1802 keV level. There is also a much larger variation in the calculated decay branching ratios of the 2^+ states between the three interactions. One possible conclusion is that the 1562 and 1802 keV states both have $J^\pi = 2^+$, but the shell model calculations are not getting the mixing between the various 2^+ states right. Another possibility is that one or both states are intruders.

The 4_2^+ state is predicted to decay primarily to the lowest two 3^+ levels, in qualitative agreement with the decay pattern observed for the 2298 keV state. However, the calculations predict a stronger branch to the 3_2^+ level, while the experimental ratio is reversed. The decay of the 2846 keV state only to the 3_2^+ level agrees significantly better with that predicted for the 4_2^+ state and poorly with that for the 3_3^+ state. The predicted energies of the 4_2^+ states lie roughly midway between 2298 and 2846 keV. Altogether, it appears more likely that the 2846 keV experimentaly state is the predicted 4_2^+ state and the 2298 keV state is not accounted for in the *sd* shell model.

The 2908 keV state decays with almost equal branches to two spin 4 states below it. A spin of 5 is strongly favored experimentally, but the theoretical 5_1^+ level is predicted to decay almost completely to the 4_1^+ state. Spin 5 was also favored experimentally for the 3464 keV state. Its exclusive decay to the lowest 4^+ state agrees well with the prediction for the 5_1^+ level. Thus the decay patterns strongly suggest that the 3464 keV state is the theoretical 5_1^+ level, but the calculated energies are closer to 2908 keV. However, the energy differences with 3464 keV are not outside the range seen for *sd* calculations, are smaller for the newer interactions, and continue the trend of generally underpredicting the experimental energies.

As discussed above, the angular distribution of its decay γ ray favors spin 6 for the 3905 keV state, while the (t,^{3}He) angular distribution [12] led to a 5^+ assignment. Although it is close in energy to the predicted 5_2^+ level, the predicted decay pattern is in total disagreement with experiment. There is partial agreement with the predicted decay pattern of the 6_1^+ level, but its energy is almost 2 MeV higher than experiment. It is also difficult to find suitable candidates in the *sd* model space for the 5510 and 6422 keV states. Their decay patterns do not resemble those predicted for the 5_3^+, 6_2^+, or 7_1^+ levels.

4.2.3 Negative-parity intruder states

Both the absence of good candidates in the *sd* shell model for some of the experimental states and the presence of negative-parity states as low as 3500 keV in ^{28}Al [29] strongly suggest

that some of the states observed in ^{30}Al have negative parity. In fact, the larger number of neutrons in ^{30}Al is likely to lower the energies for intruder states with configurations involving the $f_{7/2}$ shell.

The good agreement of the states below 1500 keV with the *sd* shell model and systematics imply that negative-parity is unlikely for for any of these states. As discussed above, the lowest 2^+ states are good candidates for the 1562 and 1802 keV levels based on energy, but the agreement in decay patterns is not very good. Since these two states decay to the 2^+ level, possible negative parities are 1^-, 2^-, and 3^-. The lowest 3^- state lies at 3591 keV in ^{28}Al. It is somewhat doubtful that this state would drop 1.8 to 2 MeV with the addition of two neutrons. and the absence of any decays to the 3^+ g.s. or any decays to the 1562 and 1802 keV states from higher lying states with higher spins make spin 3 unlikely for either state. Thus 2^+ remains most likely for these two states, but 1^- or 2^- cannot be ruled out.

Spin 4 was assigned to the 2298 keV state, but no good positive-parity candidate was identified. It appears likely that this may be a 4^- state corresponding to the lowest negative-parity state in ^{28}Al at 3465 keV. That would imply a rather reasonable drop in energy of 1167 keV. The angular distribution of its 1178 keV line implies a zero mixing ratio which is consistent with pure E1 decay (Fig. 4.14).

The 2908 keV state is a good candidate for 5^- and would imply a similar drop in energy with the corresponding state in ^{28}Al. This interpretation would explain why a low energy 608 keV transition can compete favorably with one of 1662 keV – an observation not understandable for a 5^+ state in the *sd* shell model. It is a case of a low energy M1 transition competing with a higher energy E1. In fact, the assignment of 4^- to the 2298 keV state requires negative parity for the 2908 keV state since a low energy E1 could not compete with a much higher energy M1. Also, the angular distribution of the 1662 keV decay is consistent with pure E1 decay, as is required for a 5^- assignment.

The 3905 keV state is a likely candidate for 6^-. Its decay to only higher spin states implies moderately high spin, but its decay pattern does not fit any of the reasonable positive-parity candidates. The angular distribution of its 997 keV decay line fits $6^- \rightarrow 5^-$ with a small mixing ratio (Fig. 4.16). The possible E2 branch to the 2298 keV 4^- state is also consistent. While the angular distribution of the 1605-1607 keV possible doublet shows predominantly $\Delta I = 1$ character, a weaker unresolved E2 line is not ruled out. The 5510 and 6422 keV states are likely to be 7^- since their decay angular distributions have predominantly $\Delta I = 1$

character.

To better explore the relation between the isotopes, the level schemes of ^{28,30}Al are compared in Fig. 4.17. There are some similarities in the positive-parity states, and the significant differences reflect the changing number of neutrons in the *sd* shell. However, Fig. 4.17 suggests that the main effect of the extra 2 neutrons on the negative-parity states is just a lowering of all the $\pi = -$ levels. To make this clearer, the $\pi = -$ levels in ^{28}Al have been shifted down by 1200 keV in the figure. The proposed lowest 4^-, 5^-, and 6^- states in ^{30}Al agree rather well in energy with their counterparts in ^{28}Al after the shift. Presumably this shift reflects the lower energy cost of promoting a $d_{3/2}$ neutron up to the $f_{7/2}$ shell compared to that for an $s_{1/2}$ neutron in ^{28}Al. Additional evidence comes from a comparison of the decay branches of the lowest negative-parity levels, shown in Table 4.6. There is a considerable similarity in the decay patterns for the two isotopes in spite of the $\sim$ 1.2 MeV energy difference. These comparisons cannot be extended to the 7^- states, since none are known in ^{28}Al.

Further evidence of a systematic shift in intruder energies with changing N and Z comes from a comparison of the lowest 4^- levels in the even Al (Z = 13) [30] and P (Z = 15) [31] shown in Fig. 4.18. The decrease in excitation energy of intruder configurations with both increasing N and decreasing Z is typical of "island of inversion" effects where the N = 20 shell gap decreases with increasing neutron excess. The almost identical energies for ^{28}Al - ^{30}P and ^{30}Al - ^{32}P (within 21 and 7 keV, respectively) suggest that the position of the intruder state is dependent almost entirely on N - Z.

Preparation of this graph suggested a re-examination of ^{26}Na which has been studied with essentially the same combination of reactions. The state at 2284 keV decays exclusively to the 3^+ g.s. [32], which would be consistent with 4^-. It was assigned 5^+ in the analysis of a (t,^{3}He) reaction [12]. However, a portion of that angular distribution was blocked by a contaminant, and the authors stated that the 4^- and 5^- angular distributions are very similar in shape to the 4^+ and 5^+ ones. Thus the 2284 keV state is at least a candidate for 4^-. This possibility is included in Fig. 4.18, where it fits in very nicely, differing from the corresponding level in ^{30}Al by 16 keV.

4.2.4 WBP interaction and the negative-parity states

An extended shell model space including the *sd* and *pf* shells was used to calculate the expected positions of $1\hbar\omega$ intruder states with the WBP interaction [33]. While it might be expected to give a good representation of the relative spacing of the $\pi = -$ states, their position relative to the $\pi = +$ levels may not be well predicted because of model limitations. Therefore we have shifted the predicted $\pi = -$ states down by about 1 MeV to force agreement with the lowest 4^- experimental state. These results for ^{30}Al for the $\pi = -$ states are shown in the column labeled "WBP" in Fig. 4.12. For simplicity, only the yrast and near yrast states are shown, since the in-beam experiment only populated such states. By construction the WBP interaction was designed to reproduce the USD predictions for the $\pi = +$ *sd* states, so its predictions for the $\pi = +$ levels are identical to those in the column labeled "USD". The agreement with the lowest 5^-, 6^-, and 7^- states is remarkably good, and the second 7^- level differs by 300 keV.

The WBP calculations for the lowest 4^- states in the neighboring Al isotopes are shown as a dashed line in Fig. 4.18. The calculated results were also shifted down by the same 1 MeV, as adjusted in ^{30}Al, so only the values for ^{28}Al and ^{32}Al are predictions. Not only is the decreasing trend with increasing N reproduced well, the value for ^{32}Al agrees perfectly and that for ^{28}Al, reasonably well.

4.3 SUMMARY

Complementary techniques were used to study the structure of ^{30}Al. The low-spin states were investigated following the β decay of ^{30}Mg, which was produced in the fragmentation of ^{48}Ca at the MSU NSCL. The A and Z identified fragments from the A1900 separator were correlated with subsequent β and γ decays in a DSSD. The higher-spin states were investigated at FSU in the reaction of ^{14}C on ^{18}O by observing the p-γ, p-γ-γ, d-γ, and d-γ-γ coincidences.

The β-decay experiment has located a new state at 2413 keV, given further confidence to the entire β-decay level scheme through β-γ-γ coincidences, provided firm spin assignments of 1^+ to the 688 and 2413 keV states, and determined a more accurate half life for the ground state of ^{30}Mg. The in-beam experiment at FSU has revealed for the first time the γ decay scheme of many higher-spin states. A dozen states were seen which correspond well in energy

with those previously reported in the charge exchange reaction. Four more states were seen in the present work which do not have counterparts from previous work. The γ decay modes and angular distributions provide spin assignments and restrictions for these states.

The excitation energies and decay branching ratios of the states observed in ^{30}Al were compared with the predictions of the *sd* shell model using both the older USD and newer USDA and USDB interactions. Ten states agree relatively well with the calculations and thus appear to involve pure or nearly pure *sd* structure. The RMS deviations in energy between experiment and theory for these states are 265, 175 and 173 keV, respectively. Clearly USDA and USDB provide better agreement with experiment, with no significant difference between them.

Five states whose decay patterns and energies do not agree well with the *sd* calculations are very likely negative-parity states with configurations involving one $f_{7/2}$ neutron. The proposed 4^-, 5^-, and 6^- levels agree rather well in energy with the lowest corresponding states in ^{28}Al after the ^{28}Al states are shifted down by 1200 keV. The two highest states seen appear to be 7^- states but no 7^- states are known in ^{28}Al for comparison. Calculations using the WBP interaction agree well with the negative-parity states. The decreasing energy of the intruder states with increasing neutron number fits well with the systematics of the even A Al and P isotopes. There is also a systematic decrease with decreasing proton number. This variation with N and Z is characteristic of the island of inversion, *ie* the effects of *pf* intruder configurations increase not only with increasing N as it approaches N = 20, but also decreasing Z. A very interesting relation seen is that the energy of the lowest 4^- level is almost identical for ^{28}Al and ^{32}P as well as for ^{30}Al and ^{34}P. In these cases, the 4^- energy depends only on N - Z. The relation also suggests an reassignment of 4^- to the 2284 keV level in ^{26}Na. If confirmed, this would demonstrate a sequence of 3 isotopes with constant N - Z (= 4) and almost constant 4^- energy.

Table 4.1: Gamma transitions following the β decay of ^{30}Mg

E_γ **(keV)**	**Intensity**	**Nucleus**	$E_f \rightarrow E_i$ **(keV)**
243.9(5)	100	^{30}Al	$244 \rightarrow 0$
443.9(5)	96(2)	^{30}Al	$688 \rightarrow 244$
686.8(20)	2.3(3)	^{30}Al	$688 \rightarrow 0$
1724.9(15)	6.4(8)	^{30}Al	$2413 \rightarrow 688$
2169.8(15)	3.5(5)	^{30}Al	$2413 \rightarrow 244$
1397.7(10)	2.9(5)	^{29}Al	$1398 \rightarrow 0$
2236.0(10)	65(3)	^{30}Si	$2236 \rightarrow 0$
3498.0(12)	32(5)	^{30}Si	$3498 \rightarrow 0$

Table 4.2: Gamma transitions observed in ^{30}Al in the in-beam experiment

E_x (keV)	E_γ (keV)	Intensity
243.7(5)	243.7(5)	100
687.8(5)	444.1(5)	19(2)
1120.2(10)	1120.2(10)	10(2)
	875.9 (9)	22(2)
1246.2(8)	1246.2(8)	60(3)
1562.2(12)	1318.5(15)	0.9(3)
1801.7(15)	1558.0(16)	1.8(5)
2298.4(12)	2298.4(10)	40(8)
	1178.3(28)	3.3(6)
2845.5(10)	1725.3(10)	17(2)
2907.7(13)	1661.5(14)	16(5)
	607.7(9)	37(5)
3463.6(12)	2217.4(15)	1.1(2)
3905.1(13)	997.4(13)	25(3)
	1605.1 (25)	2(1)
4292.5(11)	387.4(10)	10(1)
5510.2(25)	1605.1 (25)	8(4)
6422.1(31)	2517.0(31)	7(2)

Table 4.3: A comparison of the experimentally measured branching ratios with those predicted by the *sd* shell model using the indicated interactions. In some cases more than one possible shell model state is compared with experiment. The energies shown in the first columns are the experimental ones, while the spins and serial numbers shown in the last columns are for the theoretical states.

E_i	E_f	**Branching Ratios (%)**				J^π,#
(keV)	**(keV)**	**Exp**	**USD**	**USDA**	**USDB**	
688	244	98	100	100	100	1^+, 1
	0	2	0	0	0	
1120	244	69	73	79	71	3^+, 2
	0	31	27	21	29	
1246	0	100	100	100	100	4^+, 1
1562	1120		3	2	3	2^+, 2
	688		2	11	8	
	244	100	38	57	50	
	0		57	30	39	
1802	1120		5	7	9	2^+, 3
	688		35	1	22	
	244	100	17	6	1	
	0		44	86	68	
1802	1687		7	10	3	2^+, 4
	1562		8	3	11	
	1120		9	24	0	
	688		22	8	53	
	244	100	51	28	33	
	0		3	27	0	
2298	1246		0	0	1	4^+, 2
	1120	18	67	60	58	
	244		3	3	3	
	0	82	30	37	38	
2413	688	35	36	44	33	1^+, 2
	244	65	54	44	53	

Table 4.4: (Continued) A comparison of the experimentally measured branching ratios with those predicted by the *sd* shell model using the indicated interactions. In some cases more than one possible shell model state is compared with experiment. The energies shown in the first columns are the experimental ones, while the spins and serial numbers shown in the last columns are for the theoretical states.

E_i	E_f	Branching Ratios (%)				J^π,#
(keV)	(keV)	Exp	USD	USDA	USDB	
2846	2298		2	1	1	3^+, 3
	1802		5	3	0	
	1687		1	2	1	
	1562		3	5	3	
	1120	100	19	21	20	
	688		1	1	0	
	244		20	22	18	
	0		46	40	52	
2846	1120	100	75	70	61	4^+,2
	244		5	4	4	
	0		20	26	35	
2908	2846		0	0	0	5^+,1
	2298	57	0	0	12	
	1802		0	4	0	
	1246	43	97	94	86	
	1120		3	3	2	
	0		0	0	0	
3464	2846		8	0	5	5^+,1
	1246	100	87	90	92	
	1120		4	2	3	
	0		1	8	0	

Table 4.5: (Continued) A comparison of the experimentally measured branching ratios with those predicted by the *sd* shell model using the indicated interactions.In some cases more than one possible shell model state is compared with experiment. The energies shown in the first columns are the experimental ones, while the spins and serial numbers shown in the last columns are for the theoretical states.

E_i	E_f	**Branching Ratios (%)**				$\mathbf{J^\pi}$,#
(keV)	**(keV)**	**Exp**	**USD**	**USDA**	**USDB**	
3905	2908	> 78	1	9	3	4^+, 3
	2846		6	10	19	
	2298	< 22	0	0	0	
	1802		<1	4	6	
	1562		1	22	21	
	1246		1	6	7	
	1120		14	16	13	
	244		1	<1	<1	
	0		75	32	30	
3905	2908	>78	0	0	0	5^+, 2
	2846		0	0	0	
	2298	<22	1	0	0	
	1246		92	90	92	
	1120		1	1	1	
	0		6	9	7	
3905	2908	>78	0	1	1	4^+, 4
	2846		0	0	0	
	2298	<22	0	1	1	
	1246		1	10	15	
	1120		14	23	22	
	0		75	65	61	
3905	2908	>78	36	16	24	6^+, 1
	2298	<22	0	7	1	
	1246		64	77	75	

Table 4.6: A comparison of the negative parity decays for ^{28}Al and ^{30}Al. All energies are in keV.

^{28}Al			^{30}Al		
$E_i(J^\pi, \#)$	E_f $(J^\pi,\#)$	**Branch (%)**	$E_i(J^\pi, \#)$	E_f $(J^\pi, \#)$	**Branch (%)**
3465(4^-,1)	2272(4^+,1)	7	2298(4^-,1)		
	1014(3^+,2)	5		1120(3^+,2)	7
	0(3^+,1)	88		0(3^+, 1)	93
4033(5^-,1)	3466(4^-,1)	51	2908(5^-,1)	2298(4^-,1)	79
	2272(4^+,1)	49		1246(4^+,1)	21
5165(6^-,1)	4034(5^-,1)	100	3905(6^-,1)	2908(5^-,1)	71
				2298(4^-,1)	29

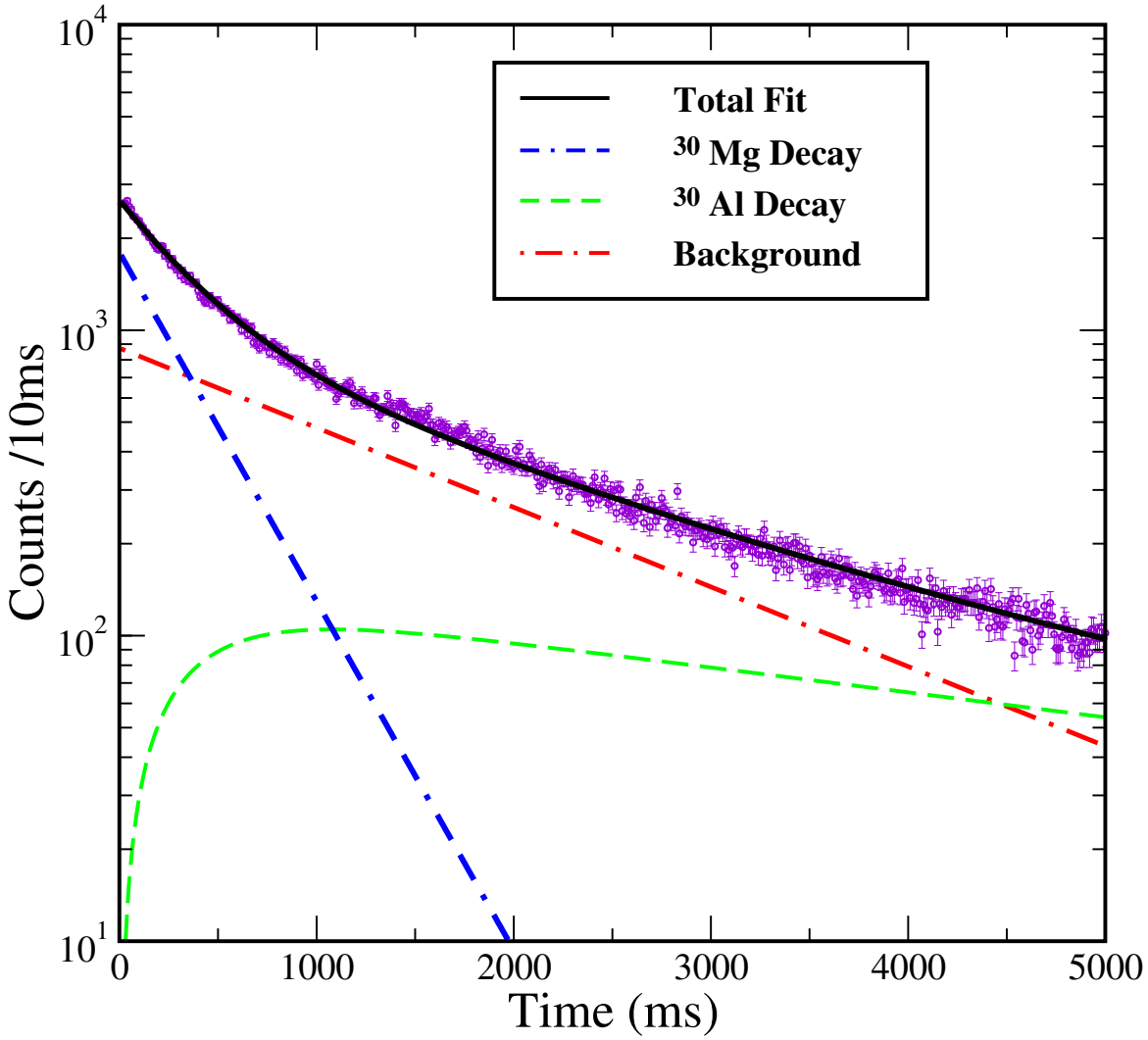

Figure 4.1: (Color online) The decay curve for ^{30}Mg. Counts per 10 s *vs.* time (ms). The half-life was determined to be 314 $\pm$ 5 ms

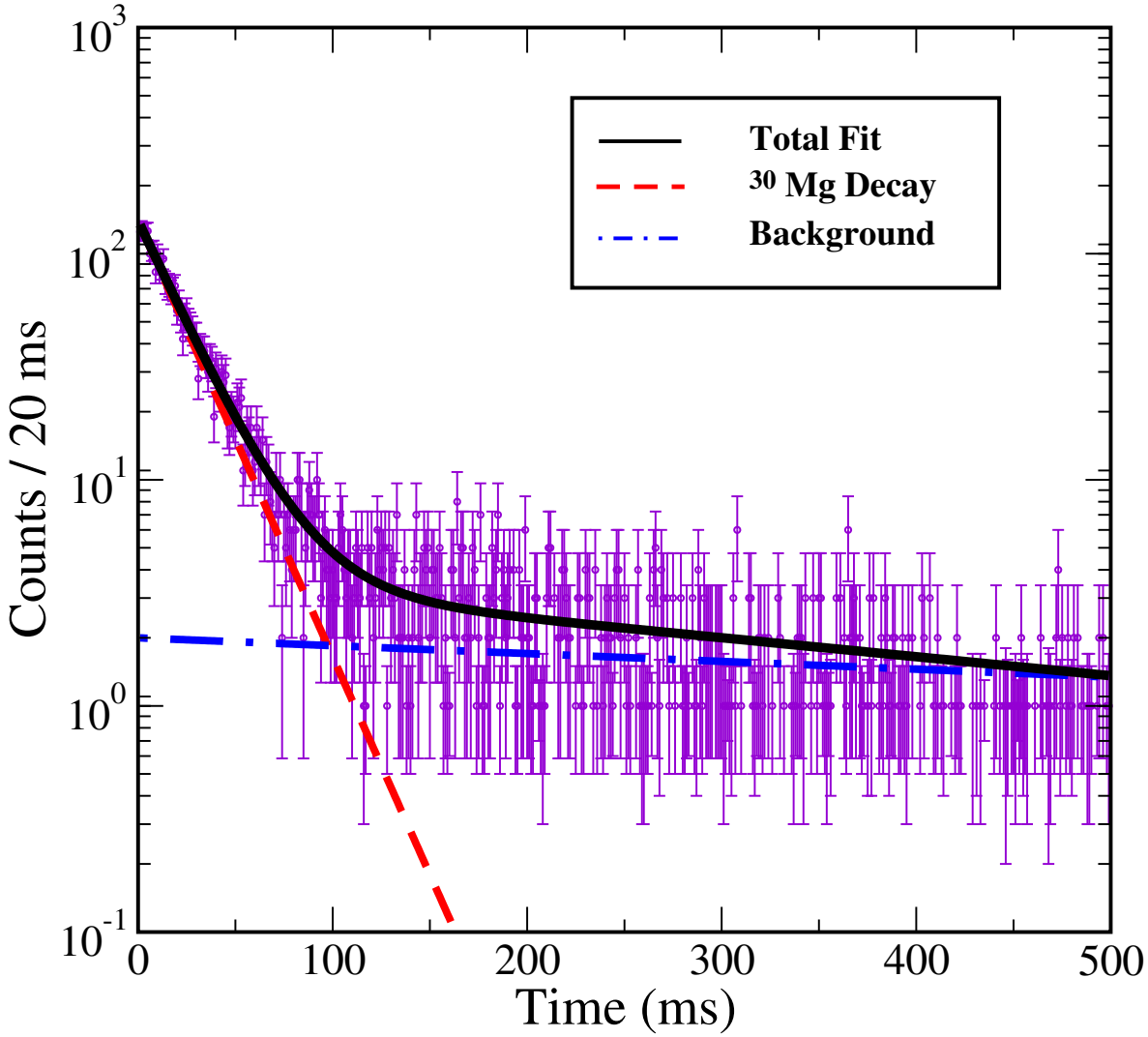

Figure 4.2: (Color online) The decay curve for the combined 244 keV and 444 keV gamma transitions. Counts per 20 ms *vs.* time (ms). The half-life was determined to be 312 $\pm$ 7 ms

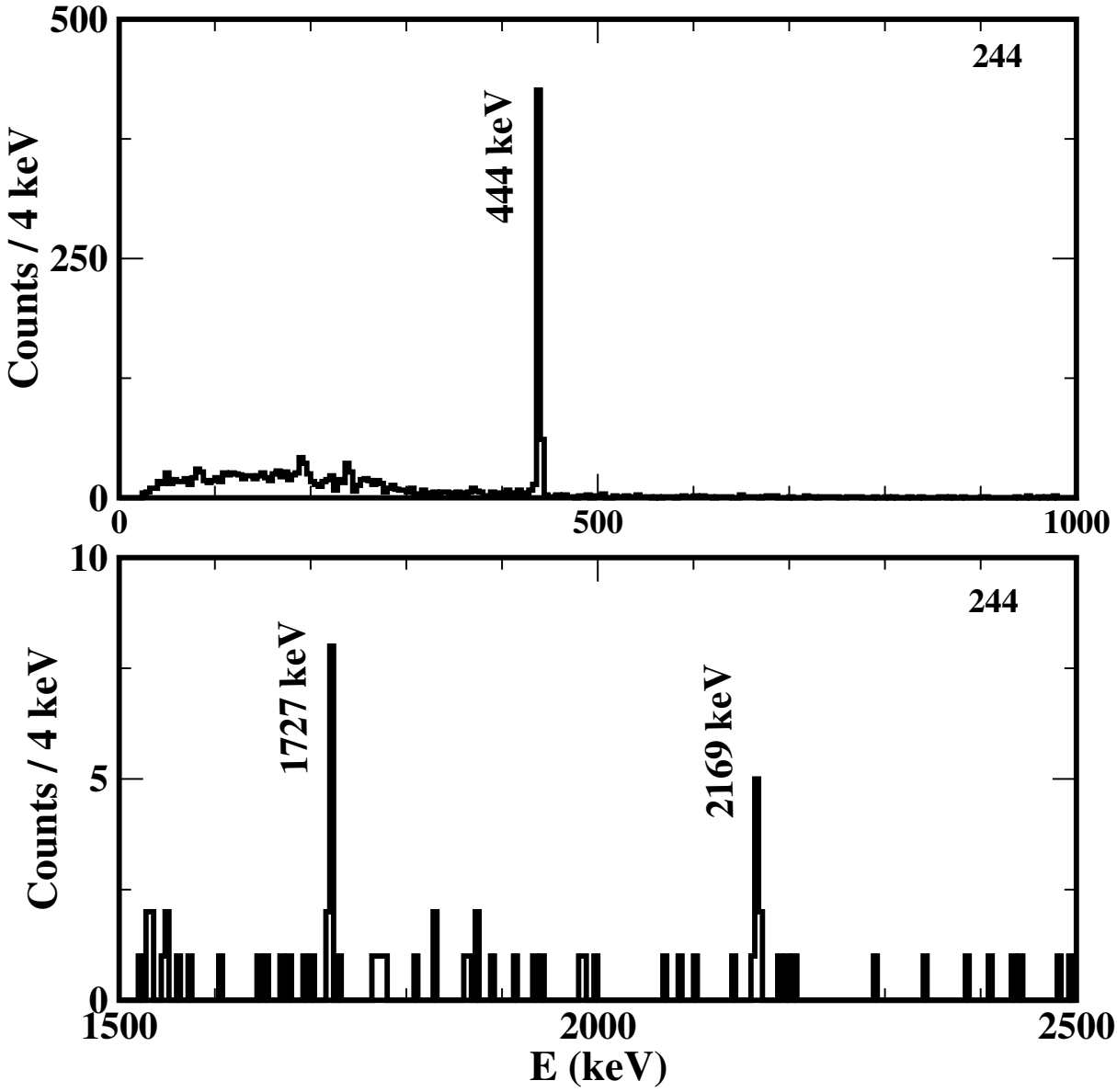

Figure 4.3: Coincidences with β's from the β-decay experiment and the 244 keV line show the known 444 keV and the two new 1725 keV and 2170 keV γ transitions

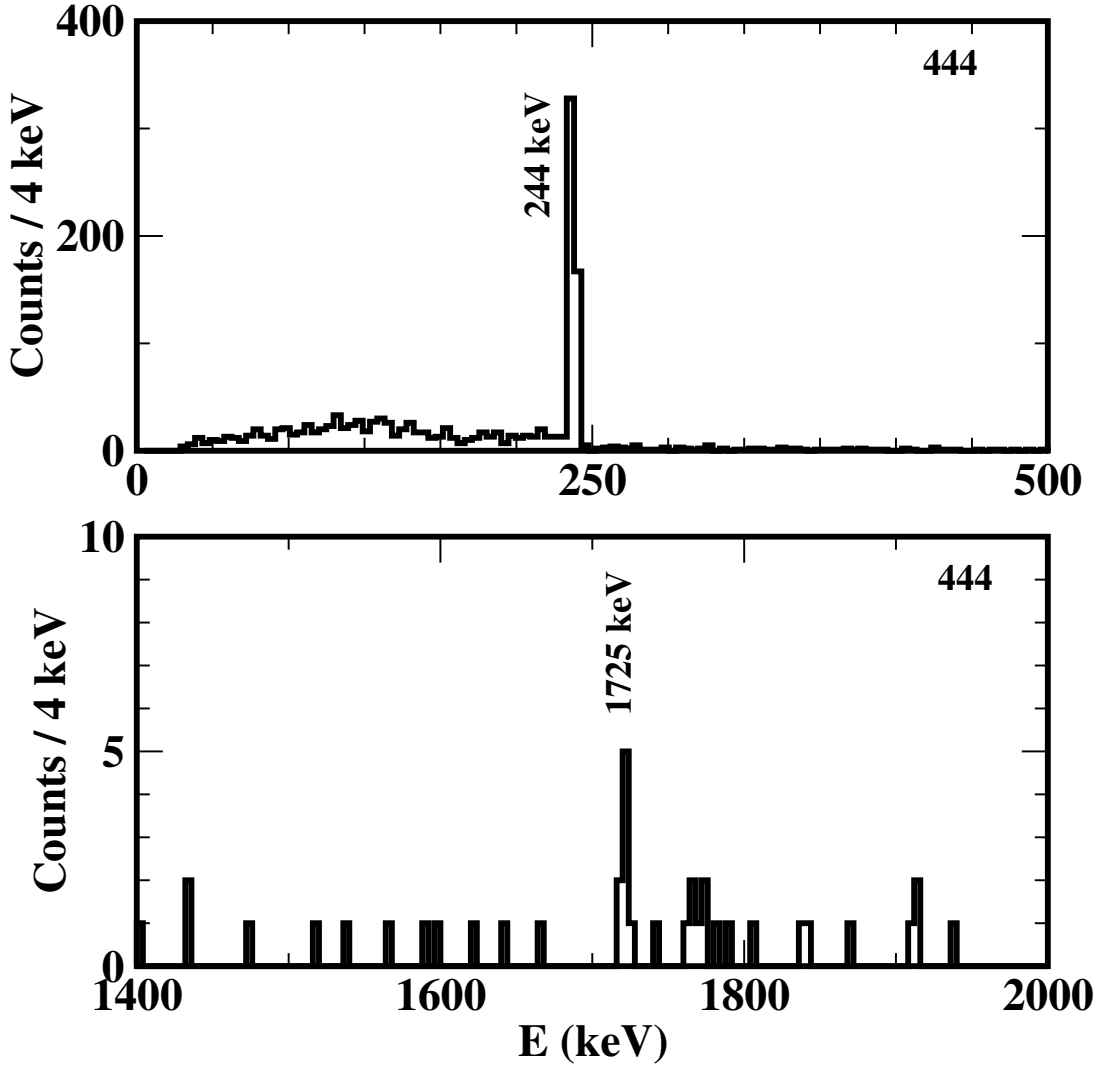

Figure 4.4: Coincidences with β's from the β-decay experiment and the 444 keV line show the known 244 keV and the new 1725 keV γ transitions.

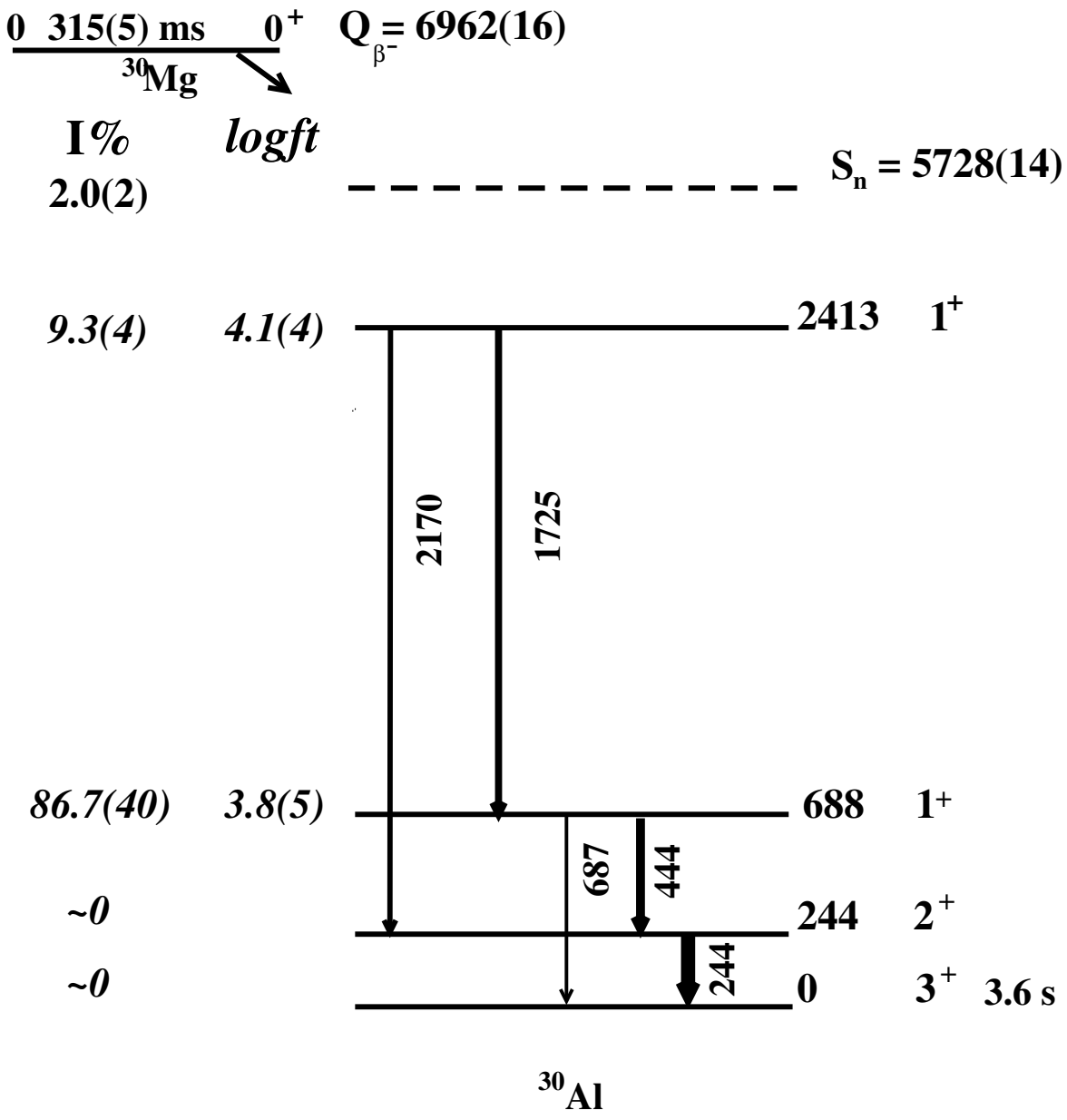

Figure 4.5: The β-decay level scheme for ^{30}Al including the two new transitions and new excited state. Transition line thickness indicates the relative intensity. All energies are in keV

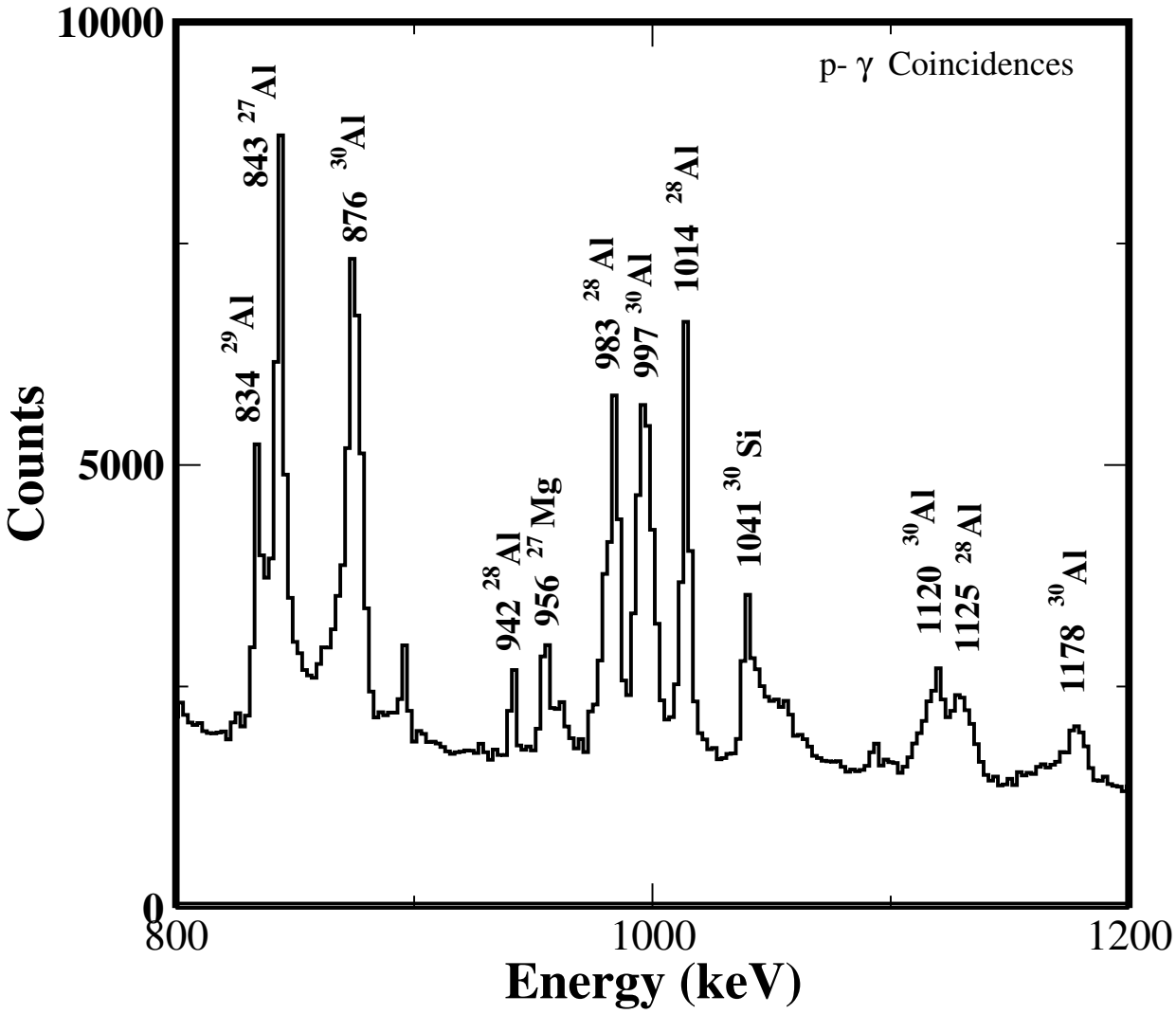

Figure 4.6: The particle-γ spectrum in the region of a reported 991 keV line.

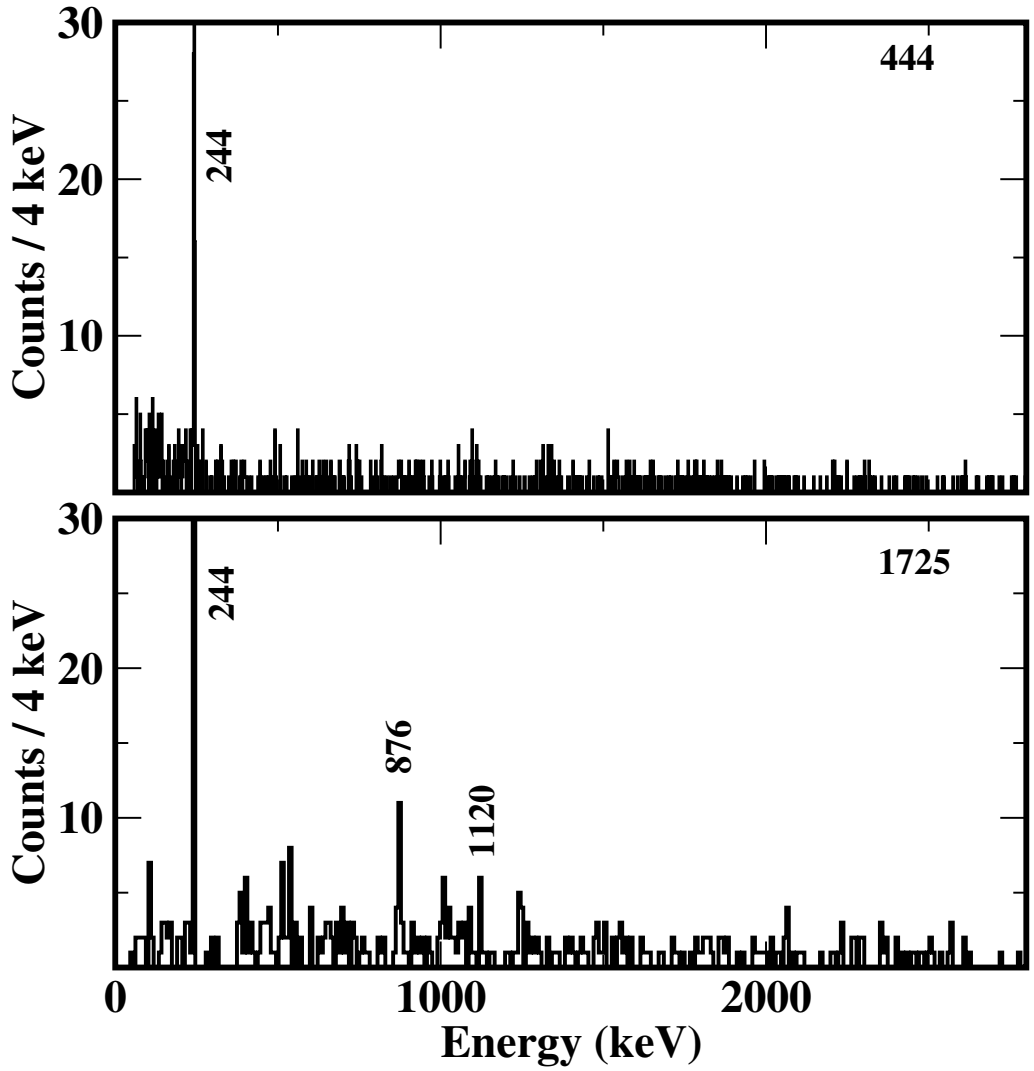

Figure 4.7: Spectra from the in-beam experiment in coincidence with protons or deuterons and the 444 keV (top) or 1725 keV (bottom) lines.

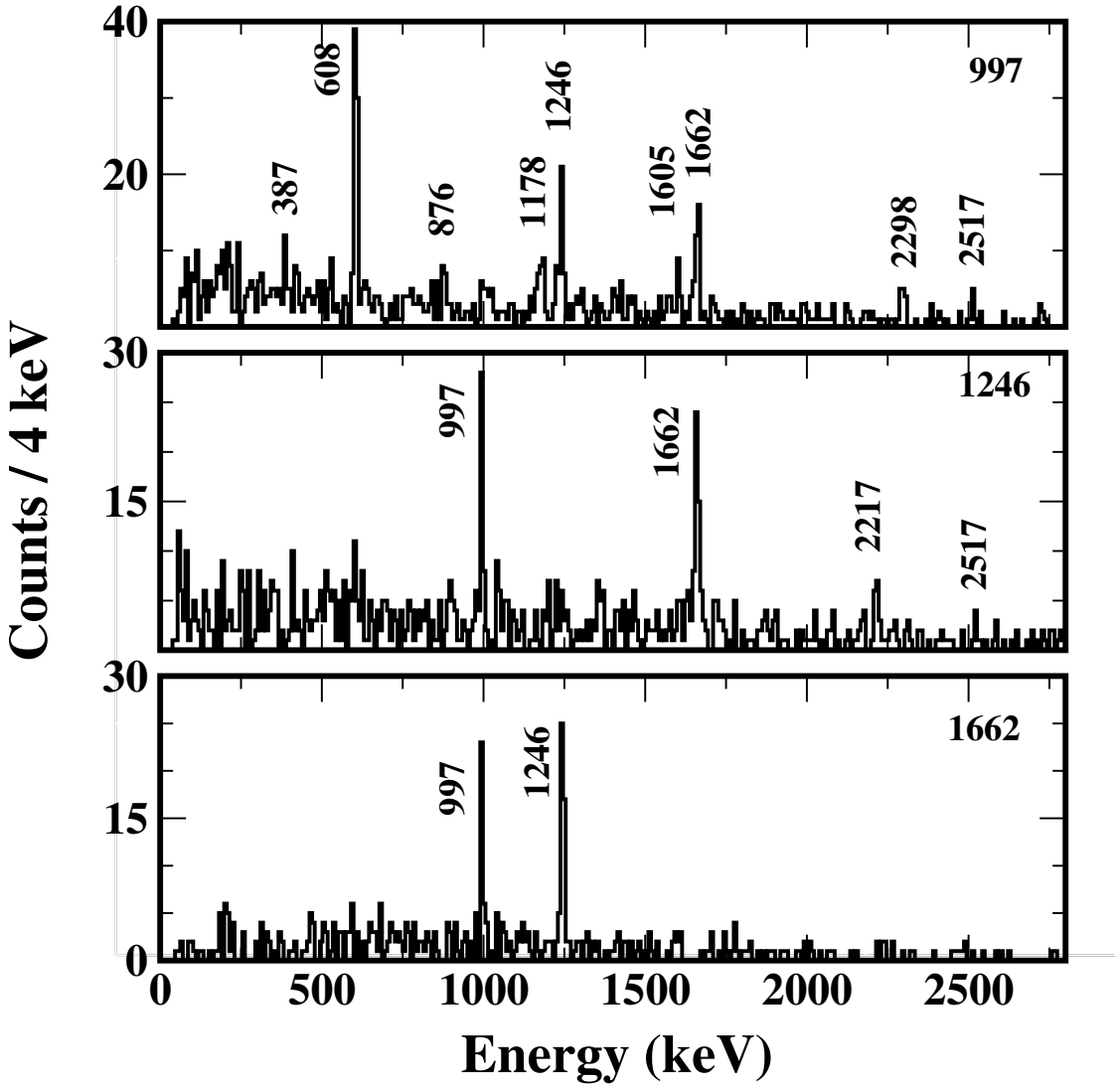

Figure 4.8: Spectra from the in-beam experiment in coincidence with protons or deuterons and the 997 keV (top), 1246 keV (middle), and 1662 keV (bottom) lines.

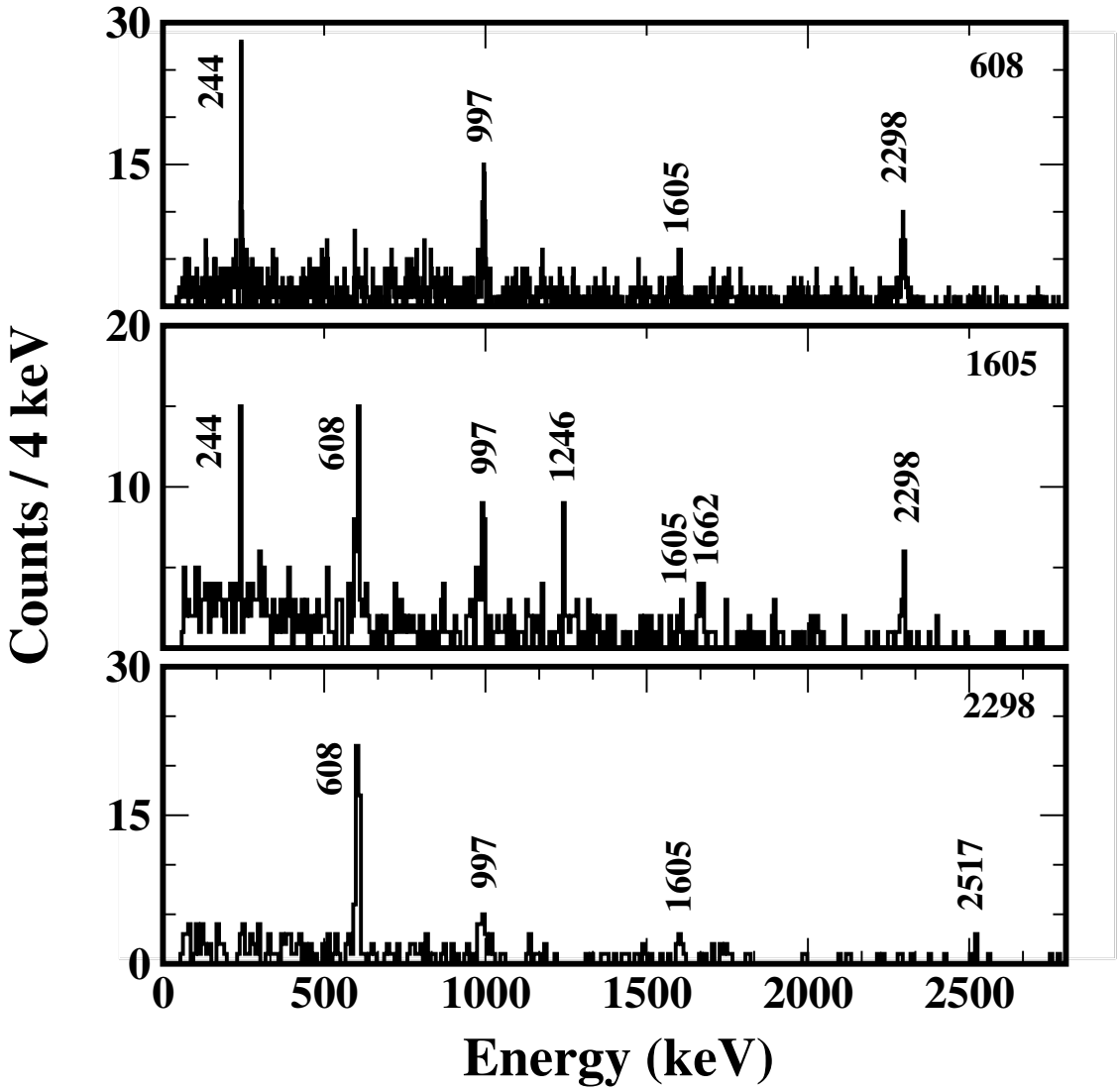

Figure 4.9: Spectra from the in-beam experiment in coincidence with protons or deuterons and the 608 keV (top), 1605 keV (middle), and 2298 keV (bottom) lines.

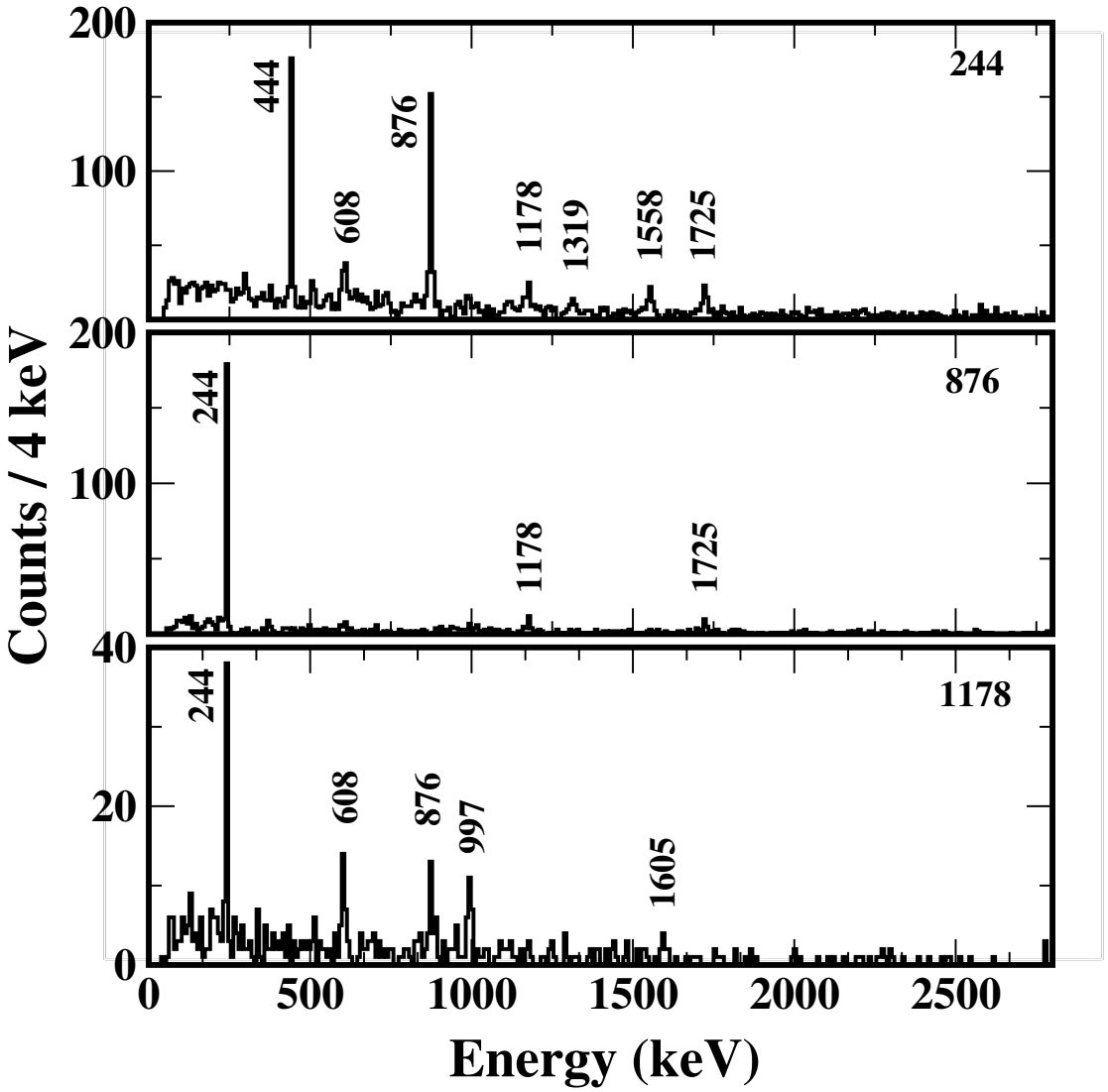

Figure 4.10: Spectra from the in-beam experiment in coincidence with protons or deuterons and the 244 keV (top), 876 keV (middle), and 1178 keV (bottom) lines.

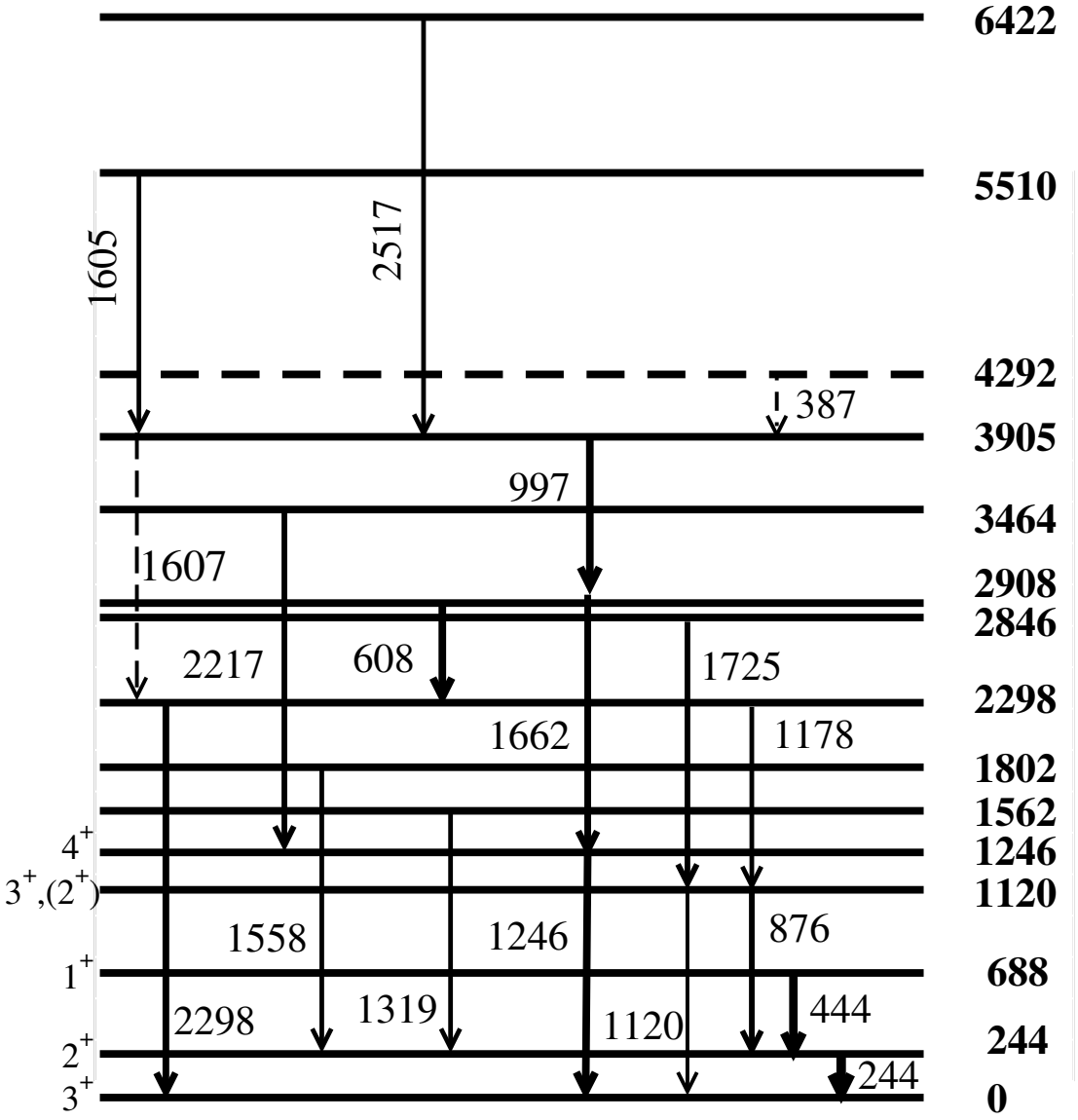

Figure 4.11: Level and decay scheme from the in-beam experiment.

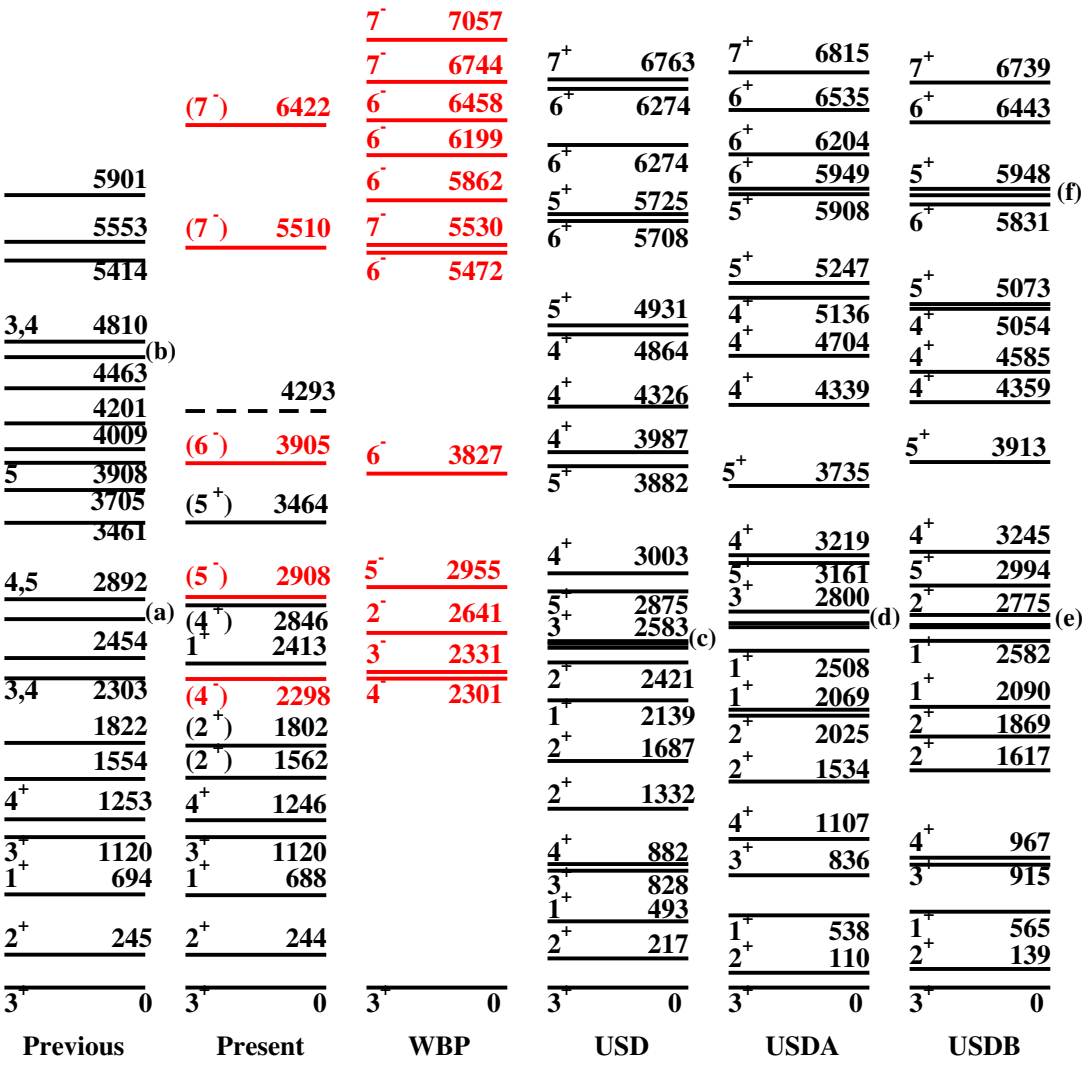

Figure 4.12: A comparison of the present results with previous experimental work and shell model calculations using the WBP, USD, USDA, and USDB interactions. Not all the predicted lower-spin states are shown above 2 MeV to reduce clutter in the figure. Levels not labeled in the figure for lack of space are (a) 2744 keV (nospin/parity assignment) (b) 4694 keV (no spin/parity assignment) (c)2538 1^+ and 2560 4^+keV, (d) 2684 keV 2^+ and 2714 keV 4^+,and (e) 2646 keV 4^+ and 2679 3^+, and (f) 5891 keV 5^+. As discussed in the text, the WBP results were shifted down by about 1 MeV.

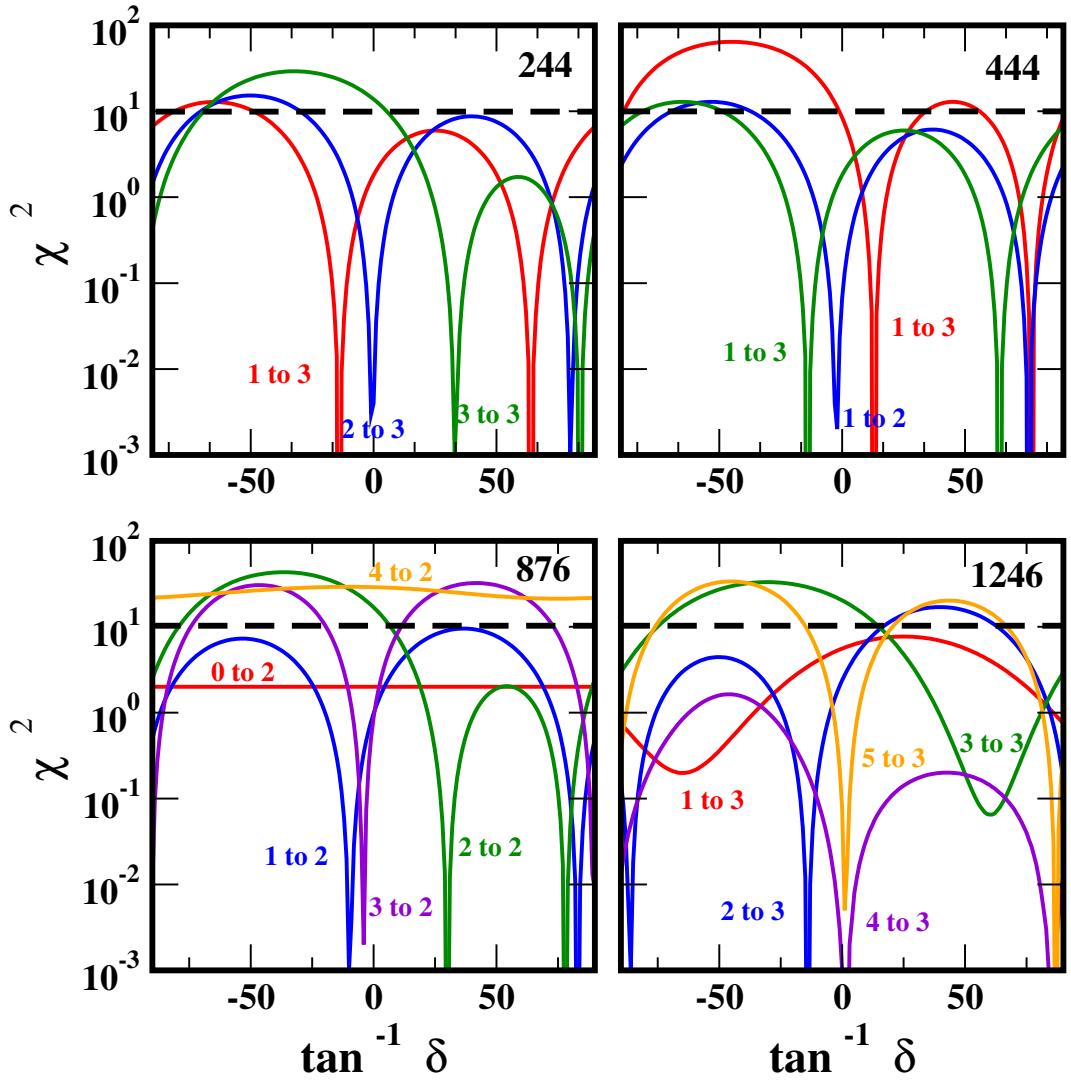

Figure 4.13: Goodness of fit χ^2 as a function of mixing ratio δ for the 244 keV, 444 keV, 876 keV, and 1246 keV transitions.

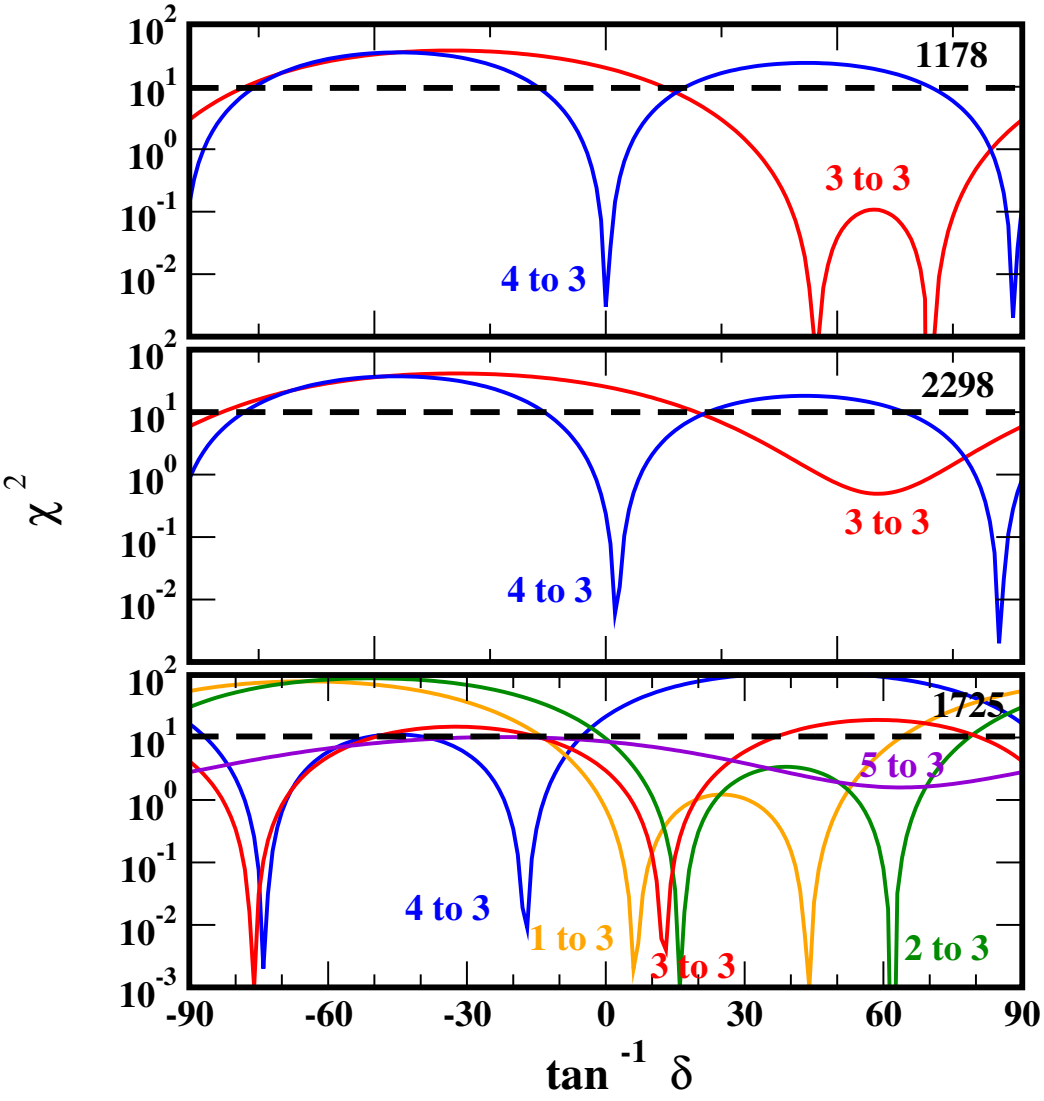

Figure 4.14: Goodness of fit χ^2 as a function of mixing ratio δ for the 1178 keV, 2298 keV, and 1725 keV transitions.

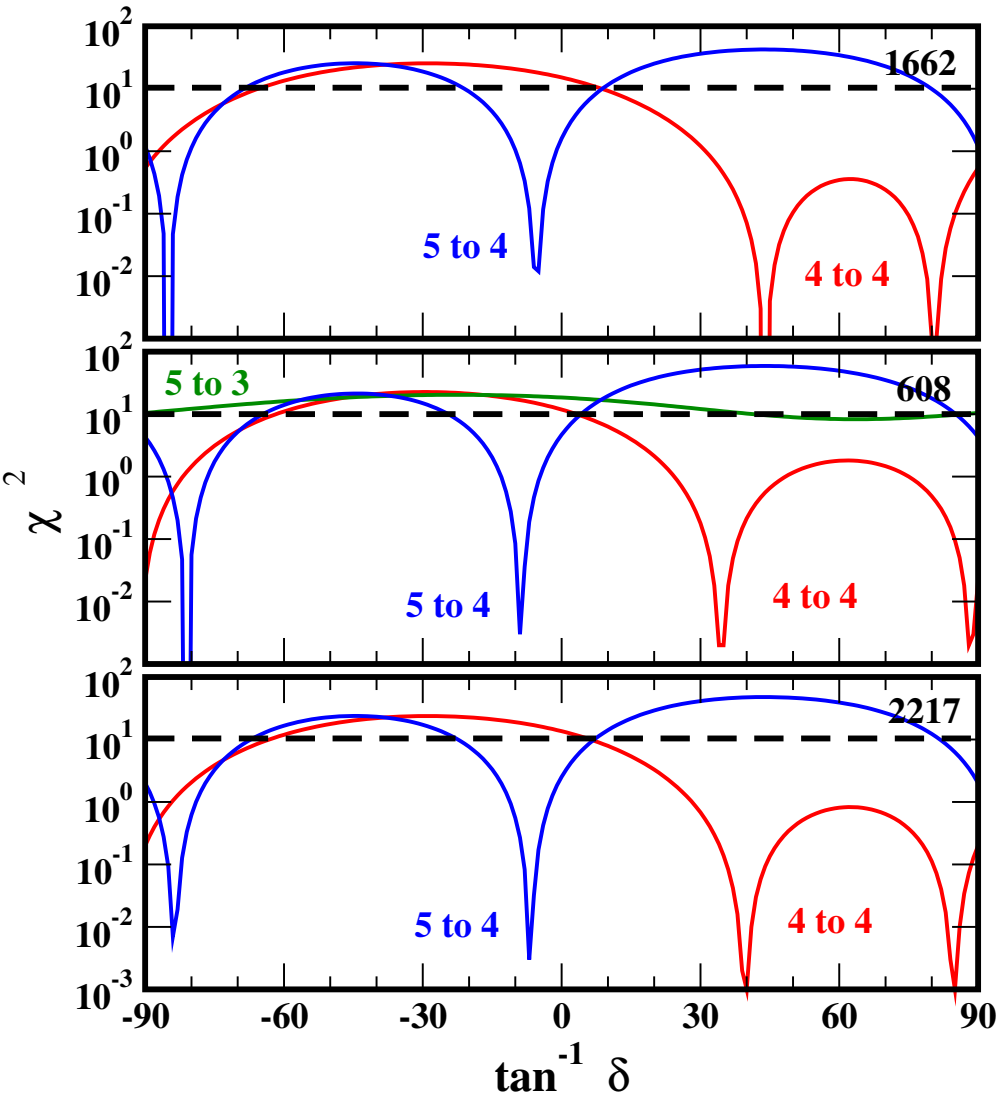

Figure 4.15: Goodness of fit χ^2 as a function of mixing ratio δ for the 1662 keV, 608 keV, and 2217 keV transitions.

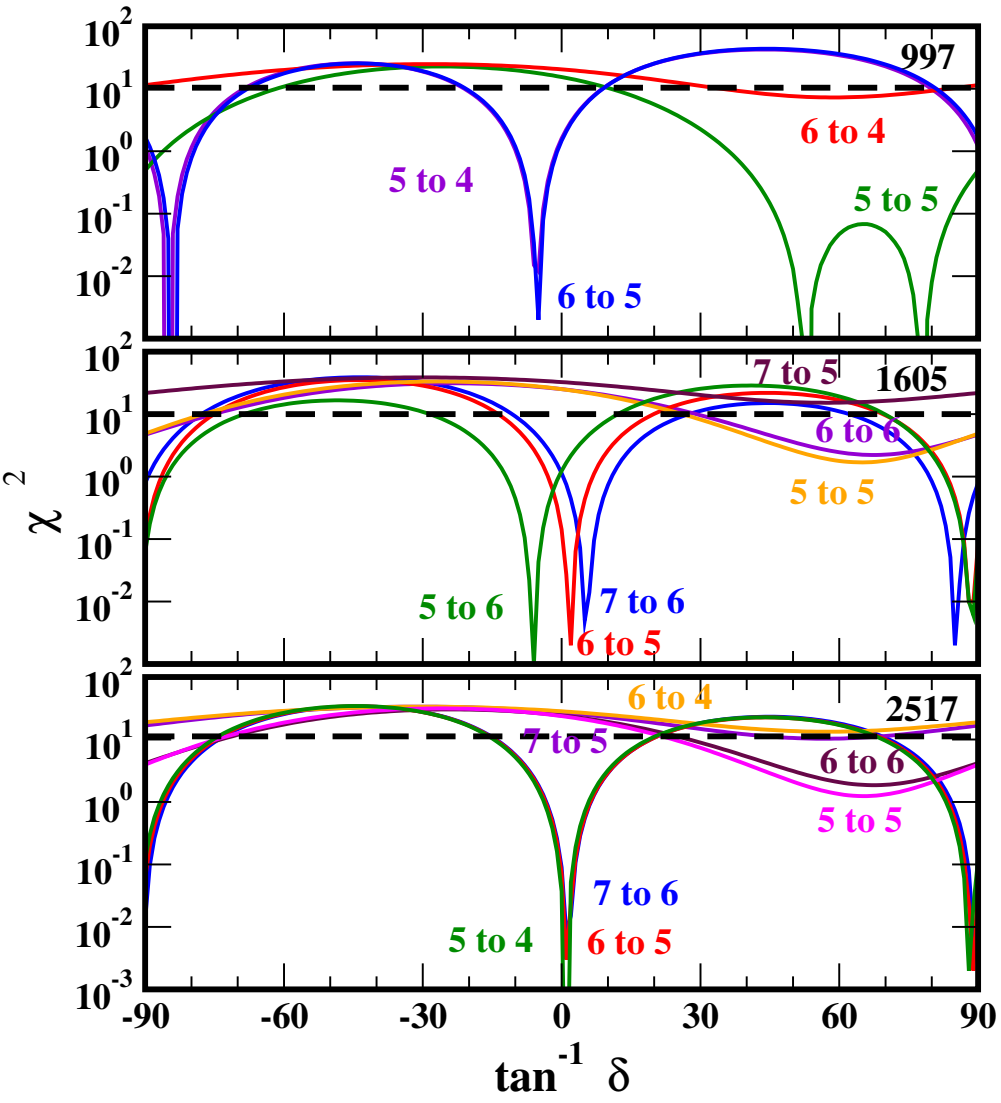

Figure 4.16: Goodness of fit χ^2 as a function of mixing ratio δ for the 997 keV, 1605 keV, and 2517 keV transitions.

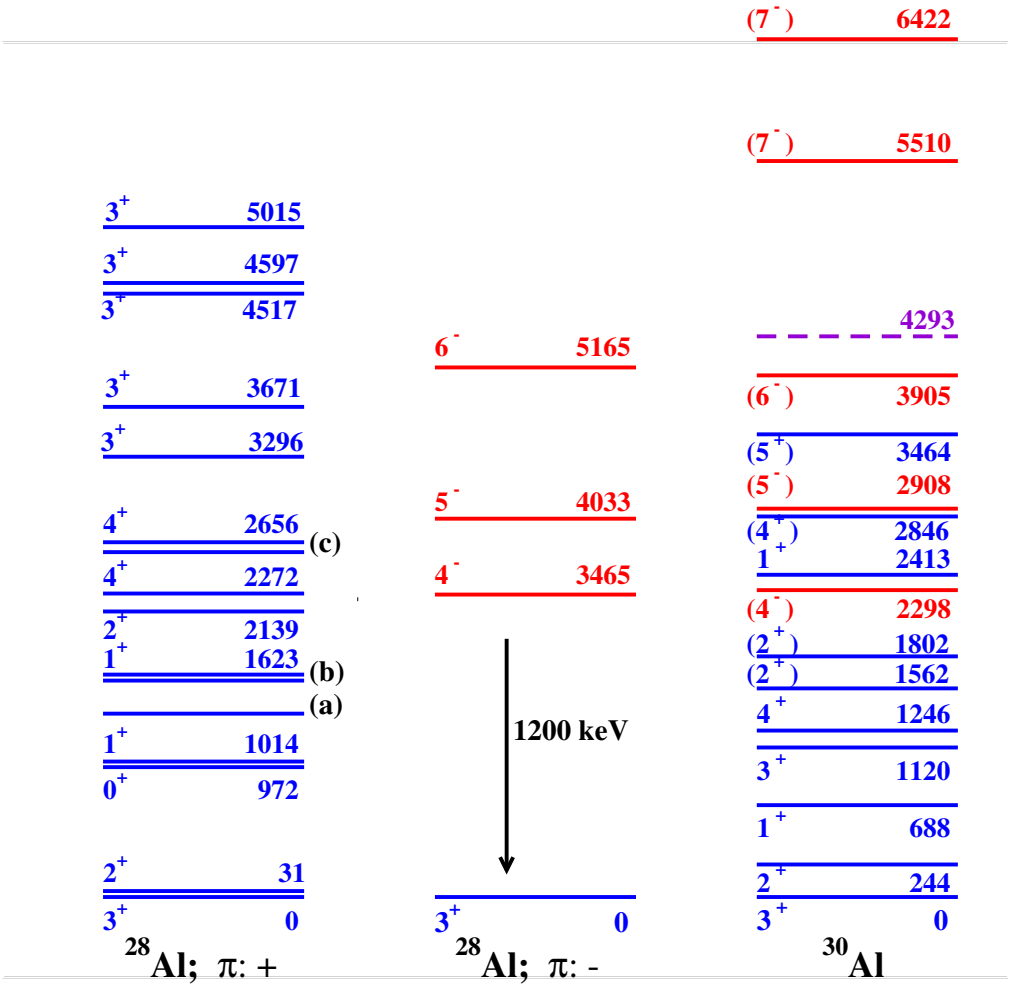

Figure 4.17: A comparison of the ^{28,30}Al level schemes. The vertical positions of the negative-parity states in ^{28}Al have been shifted down by 1200 keV, as discussed in the text. Levels not labled in the figure for lack of space are (a) 1373 keV 1^+, (b) 1620 keV 1^+, and (c) 2582 keV 5^+.

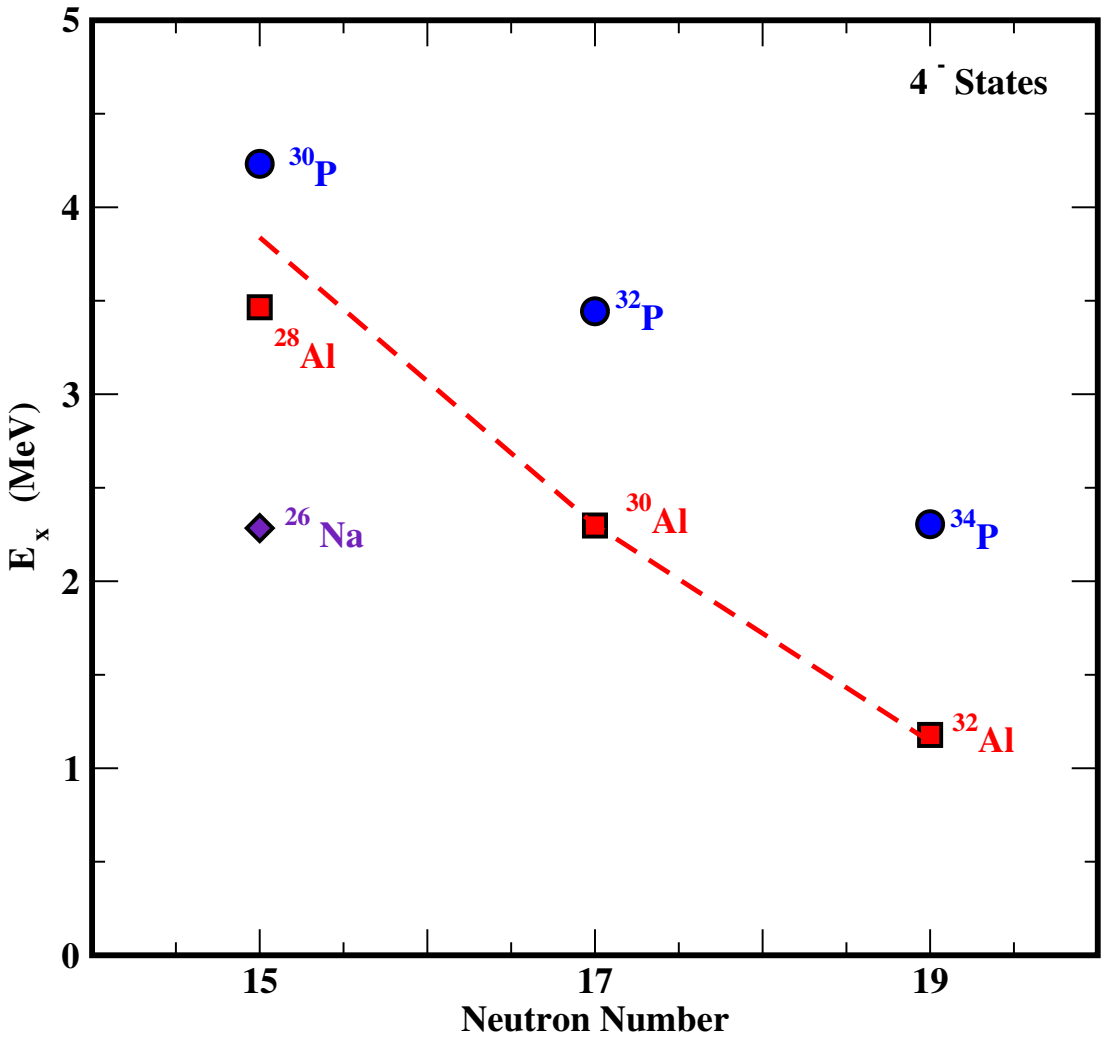

Figure 4.18: Position of the lowest 4^- states as a function of neutron number in the Z = 13 Al and Z = 15 P isotopes. The dashed line represents WBP predictions for the Al isotopes adjusted down by about 1 MeV as discussed in the text. Note that the spin-parity assignment for ^{26}Na is tentative.

CHAPTER 5

Results for ^{31}Al

5.1 RESULTS ^{31}Al

5.1.1 Half Life Measurement

The decay curve for 31Mg was created by histogramming the time differences between the identified 31Mg implant and the β decay events in the same pixel for time intervals up to 10 s. The resulting decay curve is shown in Fig. 5.1 along wit hthe fit based on the Bateman equations for the sequential growth and decay of ^{31}Mg and ^{31}Al. The decay curve was constructed using 3 components, the decay of ^{31}Mg, the growth and decay of the daughter nucleus ^{31}Al, and the background. The decay constants of ^{31}Mg and the background were allowed vary, as was the initial number of β decaying particles. A decay curve was also constructed using β-γ decay correlated implants for the 946 keV line and can be seen if Fig. 5.2. The half-life values were 227 $\pm$ 12 and 231 $\pm$ 14 for the fragment-β correlated events and fragment-β-γ correlated events, respectively. The half life obtained from this work, 229 $\pm$ 13, agrees well with the most recent experimental result of 227 $\pm$ 25 [17].

5.1.2 Level Scheme

The previously mentioned work from [17] had much better statistics than the current experiment, and therefore many more β-γ coincidences.The level scheme derived from the experiment presented in this dissertation can be seen in Fig. 5.3. Compared to [17] less states and transitions are observed resulting in different decay branching and logft values. Only a fraction of the previously observed transitions were observed.

Table 5.1: Gamma transitions following the β decay of ^{31}Mg

E_γ **(keV)**	**Intensity**	**Nucleus**	$E_f \rightarrow E_i$ **(keV)**
666(5)	42(2)	^{31}Al	$1613 \rightarrow 946$
946(5)	84(2)	^{31}Al	$946 \rightarrow 0$
1613(5)	100	^{31}Al	$1613 \rightarrow 0$
1626(8)	65(2)	^{31}Al	$3239 \rightarrow 1613$
1820(20)	13(3)	^{31}Al	$3433 \rightarrow 1613$
3196(20)	1.8(5)	^{31}Al	$4121 \rightarrow 946$
3433(15)	2.1(8)	^{31}Al	$3433 \rightarrow 0$
3620(15)	1.5(5)	^{31}Al	$3620 \rightarrow 0$

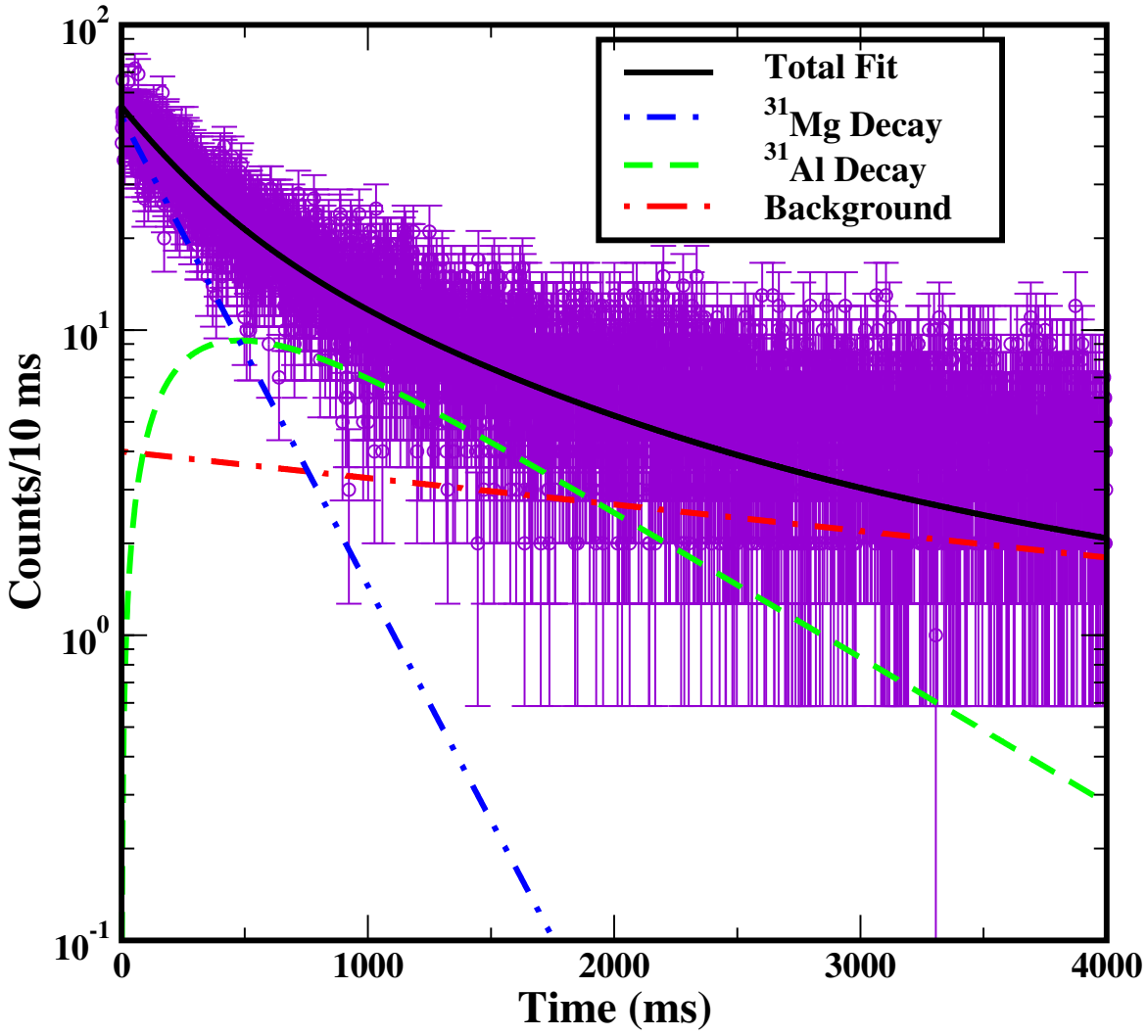

Figure 5.1: The decay curve for ^{31}Mg. Counts per 10 s *vs.* time (ms). The half-life was determined to be 227 $\pm$ 12 ms

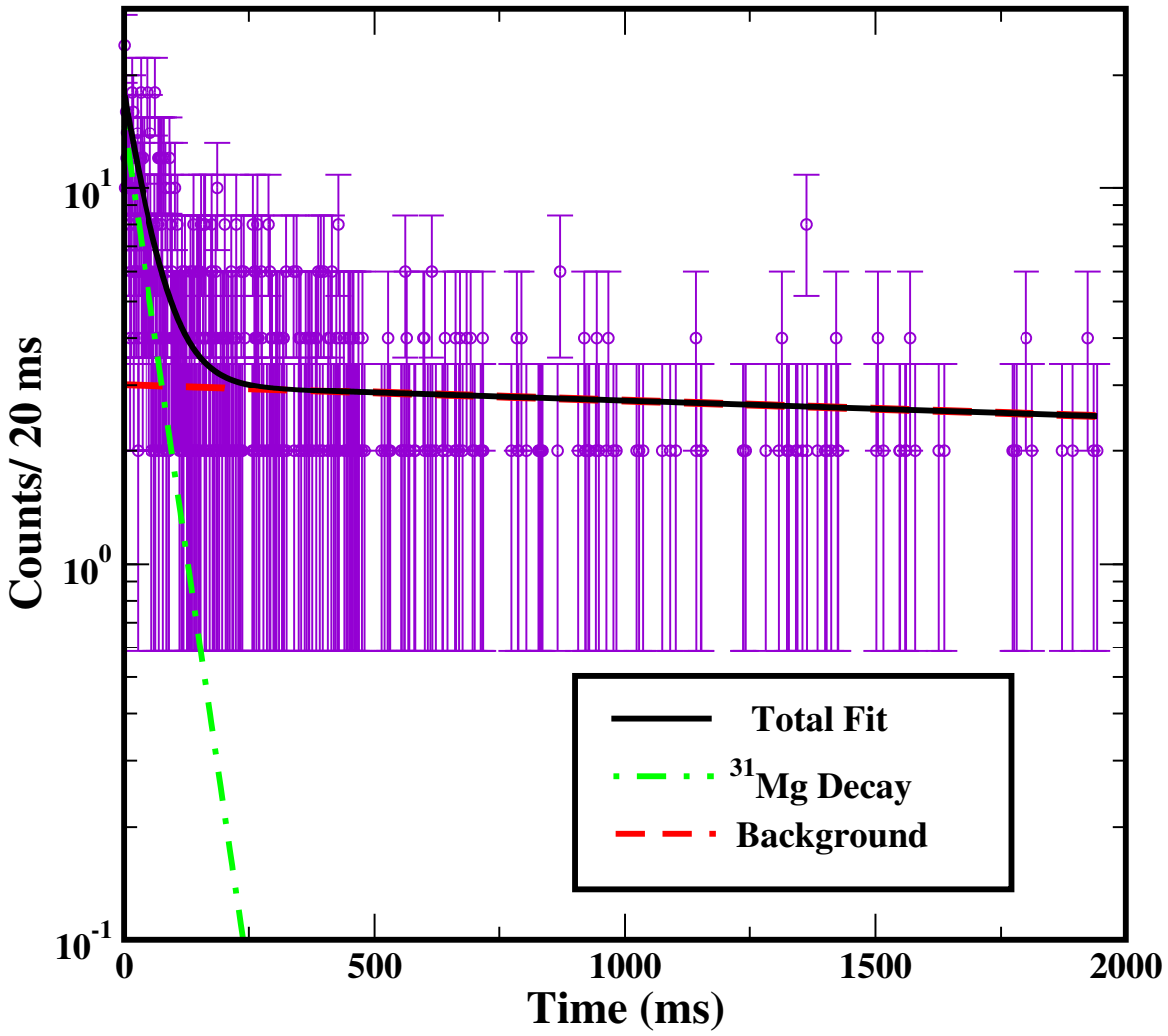

Figure 5.2: The decay curve for ^{31}Mg. Counts per 20 s *vs.* time (ms). The half-life was determined to be 231 $\pm$ 14 ms

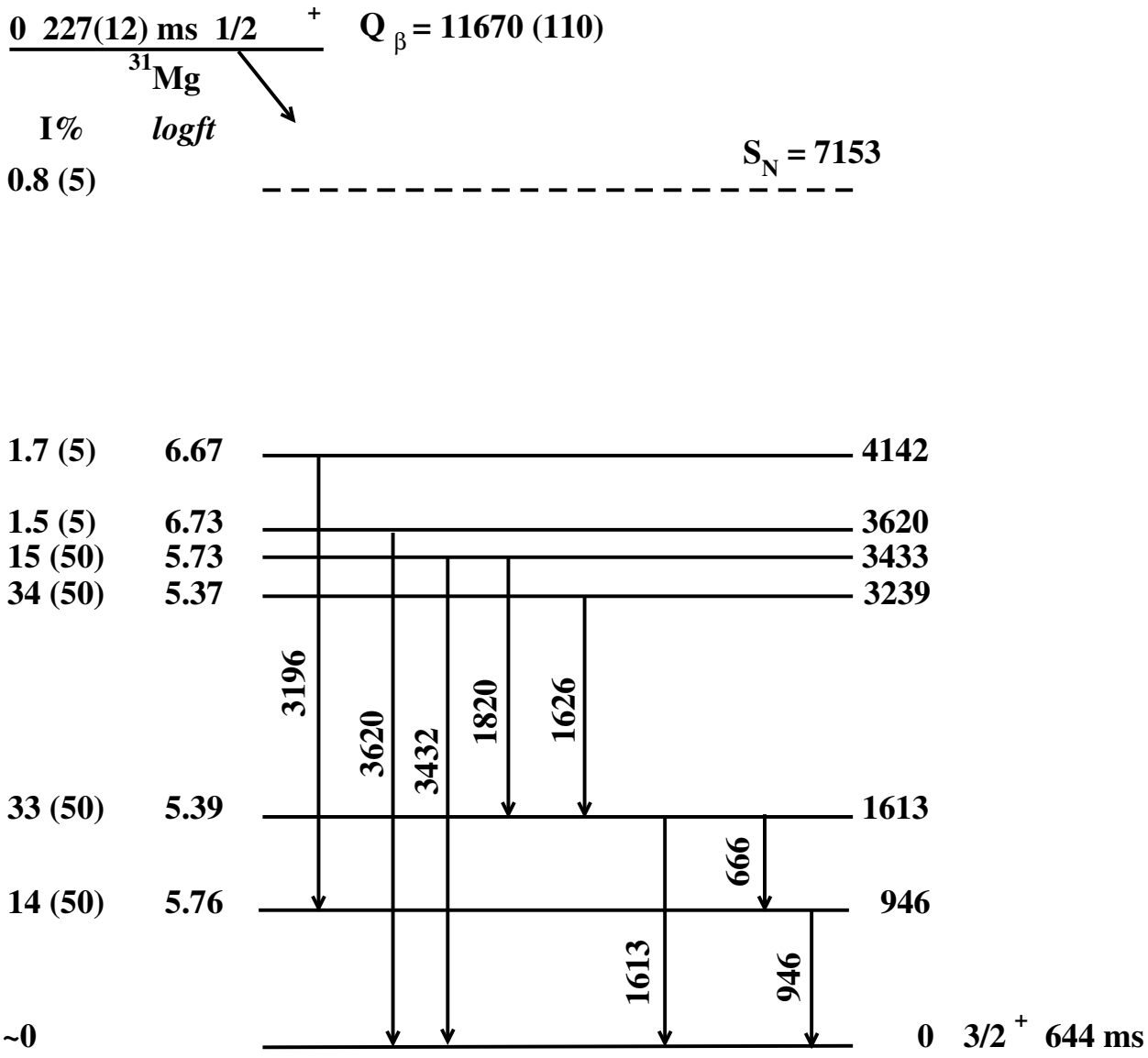

Figure 5.3: The β-decay level scheme for ^{31}Al. Transition line thickness indicates the relative intensity. All energies are in keV

CHAPTER 6

Conclusion

Complementary techniques were used to study the structure of ^{30}Al. The low-spin states were investigated following the β decay of ^{30}Mg, which was produced in the fragmentation of ^{48}Ca at the MSU NSCL. The A and Z identified fragments from the A1900 separator were correlated with subsequent β and γ decays in a DSSD. The higher-spin states were investigated at FSU in the reaction of ^{14}C on ^{18}O by observing the p-γ, p-γ-γ, d-γ, and d-γ-γ coincidences.

The β-decay experiment has located a new state at 2413 keV, given further confidence to the entire β-decay level scheme through β-γ-γ coincidences, provided firm spin assignments of 1^+ to the 688 and 2413 keV states, and determined a more accurate half life for the ground state of ^{30}Mg. The in-beam experiment at FSU has revealed for the first time the γ decay scheme of many higher-spin states. A dozen states were seen which correspond well in energy with those previously reported in the charge exchange reaction. Four more states were seen in the present work which do not have counterparts from previous work. The γ decay modes and angular distributions provide spin assignments and restrictions for these states.

The excitation energies and decay branching ratios of the states observed in ^{30}Al were compared with the predictions of the *sd* shell model using both the older USD and newer USDA and USDB interactions. Ten states agree relatively well with the calculations and thus appear to involve pure or nearly pure *sd* structure. The RMS deviations in energy between experiment and theory for these states are 265, 175 and 173 keV, respectively. Clearly USDA and USDB provide better agreement with experiment, with no significant difference between them.

Five states whose decay patterns and energies do not agree well with the *sd* calculations are very likely negative-parity states with configurations involving one $f_{7/2}$ neutron. The

proposed 4^-, 5^-, and 6^- levels agree rather well in energy with the lowest corresponding states in ^{28}Al after the ^{28}Al states are shifted down by 1200 keV. The two highest states seen appear to be 7^- states but no 7^- states are known in ^{28}Al for comparison. Calculations using the WBP interaction agree well with the negative-parity states. The decreasing energy of the intruder states with increasing neutron number fits well with the systematics of the even A Al and P isotopes. There is also a systematic decrease with decreasing proton number. This variation with N and Z is characteristic of the island of inversion, *ie* the effects of *pf* intruder configurations increase not only with increasing N as it approaches N = 20, but also decreasing Z. A very interesting relation seen is that the energy of the lowest 4^- level is almost identical for ^{28}Al and ^{32}P as well as for ^{30}Al and ^{34}P. In these cases, the 4^- energy depends only on N - Z. The relation also suggests an reassignment of 4^- to the 2284 keV level in ^{26}Na. If confirmed, this would demonstrate a sequence of 3 isotopes with constant N - Z (= 4) and almost constant 4^- energy.

The nucleus ^{31}Al was studied from the β decay of ^{31}Mg, which was produced in the fragmentation of ^{48}Ca at the MSU NSCL. The A and Z identified fragments from the A1900 separator were correlated with subsequent β and γ decays in a DSSD. A half life 229 $\pm$ 13 m for ^{31}Mg was found which agreed very well with earlier work. Through β-γ-γ coincidences, the previously known decay scheme was reproduced relatively well, although missing the more recently discovered states and transitions of [17].

REFERENCES

[1] I. Talmi and I. Unna. *Phys. Rev. Lett.*, 4:469, 1960. 1

[2] B.H. Wildenthal. *Prog. Part. Nucl. Phys.*, 11:5, 1984. 1, 2.4, 4.2.2

[3] B.H. Wildenthal M.S. Curtin and B.A. Brown. *Phys. Rev. C*, 28:1343, 1983. 1, 4.2.2

[4] L. Lessard C. Thibault R. Klapisch C. Rigaud A.M. Poskanzer R. Prieels and W. Reisdorf. *Phys. Rev. C*, 12:644, 1975. 1

[5] A.D. Davies S.N Liddick W.F. Mueller T. Otsuka A. Stolz B.E. Tomlin Y. Utsuno Vandana Tripathi S.L. Tabor P.F. Mantica C.R. Hoffman M. Wiedeking and A. Volya. *Phys. Rev. Lett.*, 94:162501, 2005. 1, 2.4

[6] P.F. Mantica A.D. Davies S.N Liddick W.F. Mueller A. Stolz B.E. Tomlin T. Otsuka Vandana Tripathi S.L. Tabor C.R. Hoffman M. Wiedeking A. Volya and Y. Utsuno. *Phys. Rev. C*, 73:054303, 2006. 1

[7] Vandana Tripathi S.L. Tabor P.F. Mantica Y. Utsuno P. Bender J. Cook C.R. Hoffman Sangjin Lee T. Otsuka J. Pereira M. Perry K. Pepper J. Pinter J. Stoker A. Volya and D. Weisshaar. *Phys. Rev. C (in press)*, 2007. 1

[8] B.A. Brown and W.A. Richter. *Phys. Rev. C*, 74:034315, 2006. 1, 2.4, 4.2.2

[9] Yutaka Utsuno Takaharu Otsuka Thomas Glasmacher Takahiro Mizusaki and Michio Honma. *Phys. Rev. C*, 70:044307, 2004. 1

[10] Ajzenberg-Selove G. Igo. *Phys. Rev. C*, 188:1813, 1969. 1

[11] K.I. Pearce N.M. Clarke R.J. Griffiths P.J. Simmonds A.C. Dodd D. Barker J.B.A England M.C. Mannion C.A. Ogilvie. *Phys. Rev. C*, 35:1617, 1987. 1, 4.1.2, 4.2, 4.2.1

[12] N.M. Clarke K.I. Pearce. *J. Phys. G: Part. Phys.*, 15:L249, 1989. 1, 4.2.1, 4.2.2, 4.2.3

[13] C. Detraz D. Guillemaud G. Huber R. Klapisch M. Langevin F. Naulin C. Thibault L.C. Carraz F. Touchard. *Phys. Rev. C*, 19:164, 1979. 1, 4.1.1, 4.1.1, 4.2.1

[14] D. Guillemaud-Mueller C. Detraz M. Langevin F. Naulin M. De Saint-Simon C. Thibault F. Touchard M. Epherre. *Nucl. Phys. A*, 426:37, 1984. 1

[15] R. L. Kozub C.B. Chitwood D.J. Fields C.J. Lister J.W. Olness E.K. Warburton. *Phys. Rev. C*, 28:2343, 1983. 1, 4.1.2, 4.2.1, 4.2.2

[16] D. Borremans et.al. *Phys. Lett*, 184B:311, 1987. 1

[17] F. Marechal et. al. *Phys. Rev. C*, 72:044314, 2005. 1, 2.4, 5.1.1, 5.1.2, 6

[18] G. Neyens M. Kowalaska D. Yordanov K. Blaum P. Himpe P. Lievens S. Mallion R. Neugart N. Vermeulen Y. Otsuka. *Phys. Rev. Lett*, 94:022501, 2005. 1

[19] Kenneth S. Krane. *Introdutory Nuclear Physics*. John Wiley and Sons, Inc., 111 River Street Hoboken NJ, second edition, 1988. 2.2, 2.3

[20] B.A. Brown and B.H. Wildenthal. *Annu. Rev. Nucl. Part. Sci.*, 38:29, 1988. 2.4, 4.2.2

[21] P. M. Endt R.B. Firestone. *Nuclear Physics*, A633:1, 1998. 2.4, 4.1.1

[22] G. Audi A. H. Wapstra and C. Thibault. *Nuclear Physics*, A792:1, 2003. 2.4, 4.1.1, 4.2.2

[23] W. Chung. *Ph.D Thesis, Michigan State University*, 1976. 2.4

[24] M. Hjorth-Jensen T.T.S. Kuo and E. Osnes. *Phys. Rep.*, 261:125, 1995. 2.4

[25] J.I. Prisciandaro A.C. Morton P.F. Mantica. *Nucl. Instrum. Methods, Phys. Res. A*, 505:140, 2003. 3.2.1

[26] G. Hackman P.G. Hansen Z. Hu K.L. Miller P. Quirin W.F. Mueller J.A. Church T. Glasmacher D. Gutknecht. *Nucl. Instrum. Methods, Phys. Res. A*, 466:492, 2001. 3.2.1

[27] J. Pavan. *Ph.D Thesis, Department of Physics, Florida State University*, 2003. 3.2.2

[28] J.P.Dufour R. Delmoral A. Fleury F. Hubert D. Jean M.S. Provikoff H. Delagrange H. Geissel K.H. Schmidt. *Z. Phys.*, A324:487, 1986. 4.1.1

[29] *http://www.nndc.bnl.gov/ensdf/*. 4.2.3

[30] S. Lunardi C. Rossi Alvarez G. Viesti G. de Angelis M. Cinausero D.R. Napoli Z.W. Grabowski B. Fornal R. Broda W. Krolas T. Pawlat J. Wrzesinski D. Bazzacco D. Fabri. *Phys. Rev. C*, 55:762, 1997. 4.2.3

[31] D.R. Napoli T. Martinez D. Bazzacco E. Farnea S. Lunardi A.G. Smith J. Ollier R. Chapman X. Liang M. Labiche K.M. Spohr M. Davison G. de Angelis M. Axioti, T. Kroll. *Phys. Rev. C*, 71:034316, 2005. 4.2.3

[32] Sangjin Lee S.L. Tabor T. Baldwin D.B. Campbell I. Calderin C. Chandler M.W. Cooper C.R. Hoffman K.W. Kemper J. Pavan A. Pipidis M.A. Riley and M. Wiedeking. *Phys. Rev. C*, 73:044321, 2006. 4.2.3

[33] E.K. Warburton and B.A. Brown. *Phys. Rev. C*, 46:923, 1992. 4.2.4

BIOGRAPHICAL SKETCH

Trisha A. Hinners

The author was born October 11, 1979 in Alton, Illinois. She graduated from Alton Senior High School in 1997. She then received her B.S. degree in Physics from Southern Illinois University Edwardsville in the spring of 2002. She fullfilled her requirements for a Ph.D. in Physics in the Spring of 2008.